Quantum simulation of an exotic quantum critical point in a two-site charge Kondo circuit

Winston Pouse[1,2,3†], Lucas Peeters[3,4†], Connie L. Hsueh[1,2,3], Ulf Gennser[5], Antonella Cavanna[5], Marc A. Kastner[2,4,6], Andrew K. Mitchell[7,8*], and David Goldhaber-Gordon[2,4*]

[1]Department of Applied Physics, Stanford University, Stanford, CA 94305, USA
[2]Stanford Institute for Materials and Energy Sciences, SLAC National Accelerator Laboratory, Menlo Park, California 94025, USA
[3]Geballe Laboratory for Advanced Materials, Stanford University, Stanford, California 94305, USA
[4]Department of Physics, Stanford University, Stanford, CA 94305, USA
[5] Centre de Nanosciences et de Nanotechnologies (C2N), CNRS, Univ. Paris-Sud, Université Paris-Saclay, 91120 Palaiseau, France
[6]Department of Physics, Massachusetts Institute of Technology, Cambridge, MA 02139, USA
[7] School of Physics, University College Dublin, Belfield, Dublin 4, Ireland
[8] Centre for Quantum Engineering, Science, and Technology, University College Dublin, Belfield, Dublin 4, Ireland

† These authors contributed equally to this work.
*To whom correspondence should be addressed;
E-mail: andrew.mitchell@ucd.ie, goldhaber-gordon@stanford.edu.

***Abstract*—Tuning a material to the cusp between two distinct ground states can produce physical properties that are unlike those in either of the neighboring phases. Advances in fabrication and control of quantum systems has raised the tantalizing prospect of artificial quantum simulators that can capture such behavior. A tunable array of coupled qubits should have an appropriately rich phase diagram, but realizing such a system with either tunnel-coupled semiconductor quantum dots or metal nanostructures has proven difficult. The challenge for scaling up to clusters or lattices is to ensure that each element behaves essentially identically and the coupling between elements is uniform, while also maintaining tunability of the interactions. In this work, we study a nanoelectronic circuit comprising two coupled hybrid metal-semiconductor islands, combining the strengths of both materials to form a potentially scalable platform. The semiconductor component allows for controllable inter-site couplings at quantum point contacts, while the metal component's effective continuum of states means that different sites can be made equivalent by tuning local potentials. The couplings afforded by this architecture can realise an unusual quantum critical point resulting from frustrated Kondo interactions. The observed critical behaviour matches theoretical predictions, verifying the success of our experimental quantum simulation.**

INTRODUCTION

The rich behaviors of bulk materials emerge from microscopic quantum interactions among their many electrons and atoms. When competing interactions favor different collective quantum states, one can often tune from one quantum state to another by applying pressure, electromagnetic fields, or chemical doping. In principle this can even happen at absolute zero temperature: a *quantum phase transition* [1, 2]. Remarkably, the zero-temperature quantum critical point (QCP) at a specific value of a tuning parameter controls behavior over a widening range of parameter values as the temperature is increased, making signatures of criticality experimentally accessible. Further, seemingly very different systems can behave in the same 'universal' way near their respective critical points.

A full microscopic description of the range and character of different phases and the transitions between them is in most cases impossible, given the sheer chemical complexity of real bulk materials. Fortunately, simplified models often capture the essential physics of interest, providing valuable insight into the behavior of bulk materials and even guiding design of new materials. Typically, these models describe a set of local sites, each hosting one or a few interacting quantum degrees of freedom, coupled to other sites and sometimes to conducting reservoirs [3]–[6]. Calculating the low-energy properties of even these simplified models on clusters of more than a few sites exceeds the capabilities of the most powerful classical computers. Digital quantum computers could work for such calculations, but only once they are scaled to a far greater number of quantum bits than the present state of the art. Highly tunable nanoelectronic circuits based on one or a few semiconductor quantum dots can act as analog quantum simulators, directly implementing Hamiltonians of interest and thus offering the near-term prospect of more powerful computation than other currently available approaches. These circuits display diverse phenomena including Coulomb blockade [7], various Kondo effects [8]–[15], emergent symmetries [16, 17], and fractionalization [18]–[21]. Quantum phase transitions with universal properties have also been realized in such circuits [18]–[20, 22, 23].

However, the circuits studied so far cannot fully capture collective behavior over many sites of a lattice [24, 25]. A long-standing goal is to scale up these circuits to more directly mirror the structure of bulk materials. For example, a four-site Fermi-Hubbard system was recently studied using semi-automated control and tuning capabilities [26], but scaling up to a larger uniform lattice is daunting. Even with advanced modern fabrication, disorder in doping and lithographic patterning can make the level spectra of two nominally identical quantum dots inequivalent [27]. An array of gates may be used to equalize local chemical potentials across different sites, but many-body ground states are still affected by the full level spectrum of each site [28], which cannot be fully controlled in these systems.

A recently-introduced paradigm for quantum simulation of quantum phase transitions is based on a local site formed from a hybrid metal-semiconductor island [19, 20]. Here we demonstrate that this approach is uniquely advantageous for scaling to larger arrays: because the metal component hosts an effective continuum of single particle states, different islands of the same size behave essentially identically. As a step toward scaling up such systems, the nature of the coupling between neighboring islands must be understood. In this article, we develop a model to describe the coupling between islands in the simplest two-site system, and validate this model experimentally using transport measurements. We show that this device architecture generates an inter-site interaction that favors a many-body coherent state in which the islands are collectively screened by each other, and become strongly entangled by a charge-Kondo effect. This interaction competes with the usual island-lead interactions [19], which favor separate Kondo screening of each island by its attached lead [29]. The frustration between these interactions in a system of two *identical* sites results in a QCP. Measured conductance signatures across the quantum phase transition – which is a variant of the long-sought two-impurity Kondo (2IK) transition [30] – match universal theoretical predictions for our model. Scaling up to many such coupled sites will allow experimental simulation of lattice models that are beyond the reach of traditional computational techniques.

Our device consists of a circuit containing two coupled hybrid metal-semiconductor islands, each also coupled to its own lead, as illustrated schematically in Fig. 1a. Even though the islands are small enough to have a substantial charging energy, the metal component endows each island with an effective continuum of single particle states. This contrasts with the discrete and individualized level spectrum of pure semiconductor quantum dots noted above. Our circuit is based on a GaAs/AlGaAs heterostructure which hosts a buried two-dimensional electron gas (2DEG). Mesas are lithographically patterned (blue regions in Fig. 1a, outside

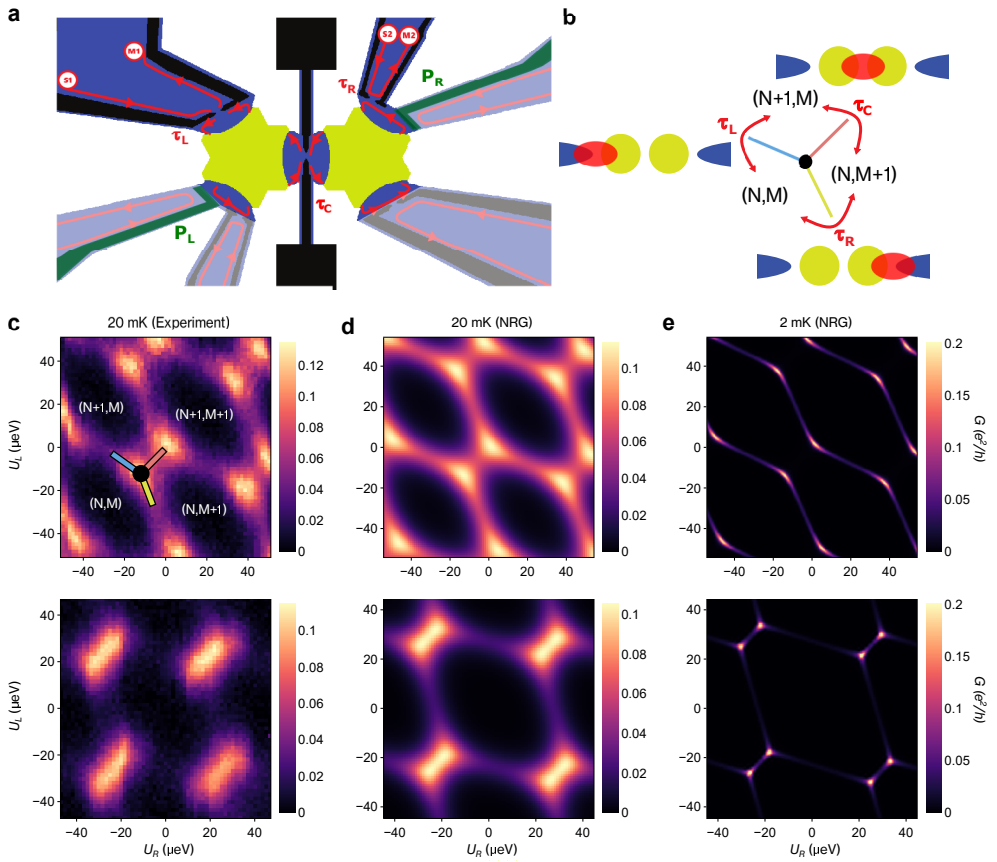

Fig. 1: Two island charge-Kondo device. a, Schematic layout of the device structure, consisting of two metal components (yellow-green) coupled to quantum Hall edges (red lines) in a buried 2DEG (blue) via QPCs (black). The island constitutes the metal component and the three surrounding patches of 2DEG on the inner side of the three QPCs. Only the top and central QPCs are used throughout this work. The island levels are controlled via plunger gates (green). **b,** Three neighbouring charge states are interconverted by direct tunneling of electrons at each of the three QPCs, characterized by transmissions τ_L, τ_R, τ_C. Distinct Kondo effects (illustrated as red ovals) arise along each two-state degeneracy line. At the triple point connecting them, the three different Kondo interactions cannot simultaneously be satisfied, leading to frustration and a quantum critical point. **c, d,** Experimentally measured series conductance and NRG calculations at 20 mK for $\tau_L = \tau_R \equiv \tau = 0.38$ ($J_L = J_R \equiv J = 0.35$) as the island potentials U_L, U_R are varied via plunger gate voltages P_L and P_R. The top row corresponds to $\tau_C = 0.9$ ($J_C = 0.5$) and the bottom row $\tau_C = 0.7$ ($J_C = 0.3$). The bright conductance spots in the top row correspond to the triple points. In the bottom row, the triple points are closer and somewhat merged. **e,** NRG calculated stability diagram at the experimentally inaccessible temperature of 2 mK for the same settings as in **d**. Theory predicts clear Kondo-enhanced peaks at the triple points, with Kondo-suppressed conductance elsewhere.

of which the 2DEG is etched away). The metal components are deposited bridging the various mesas, then are electrically connected to the 2DEG by thermal annealing. The combination of metal and three surrounding patches of 2DEG form the hybrid metal-semiconductor island. The device is operated in a magnetic field of 4.3 T, corresponding to a quantum Hall filling factor 2 in the 2DEG bulk; this provides robust, spin-polarized conduction electron channels. The left and right islands are designed to behave identically: the spacing of single-particle states on each island is far below $k_B T$ at our base temperature of 20 mK; and their charging energies $E_C^L \approx E_C^R \approx 25$ μeV are equal to our experimental resolution ($I \approx 10$ μeV is the inter-island capacitive interaction). Lithographically patterned metallic top gates form quantum point contacts (QPCs, black in Fig. 1a). The transmissions τ_L and τ_R control the left and right island-lead tunnel couplings, while τ_C controls the coupling between the islands. Each coupling is through the outermost quantum Hall edge state; QPC voltages are set so that the second, inner channel, is completely reflected. Throughout the experiment we fix $\tau_L = \tau_R \equiv \tau$ and keep all other QPCs closed. Finally, plunger gates (green) control the electrostatic potential, and hence electron occupancy, on each island. We measure the conductance G from left lead to right lead through both islands in series, as a function of the left and right plunger gate voltages P_L and P_R. See Methods for further details of the device and measurement setup.

We now formulate a model to describe our two-site device at low temperatures below the island charging energies, and when the QPCs are only partially open (that is, when $k_B T \ll E_C^{L,R}$ and $\tau, \tau_C < 1$). Our low-energy effective model retains only the lowest two macroscopic charge states of each island ($n = N$ or $N+1$ electrons on the left island and $m = M$ or $M+1$ electrons on the right island), giving four thermally accessible charge configurations (n, m) for the two sites,

around a single pair of degenerate triple points (see the experimental charge stability diagram in Fig. 1c, discussed further below). Virtual excitations to higher charge states are neglected. The two-level systems of retained charge states on each island are mapped to charge pseudospins in the effective model, which then takes the form of a modified two-impurity Kondo model. The derivation (see Methods and Supplementary Information) follows along similar lines to that of the charge-Kondo mapping for a single island introduced theoretically by Matveev and coworkers [29, 31, 32], and validated experimentally by Iftikhar and coworkers [19, 20]. Our proposed double charge-Kondo (DCK) model reads,

$$H_{\mathrm{DCK}} = \Big(J_L \hat{\mathcal{S}}_L^+ \hat{s}_L^- + J_R \hat{\mathcal{S}}_R^+ \hat{s}_R^- + J_C \hat{\mathcal{S}}_L^+ \hat{\mathcal{S}}_R^- c_L^\dagger c_R + \mathrm{H.c.} \Big) + I \hat{\mathcal{S}}_L^z \hat{\mathcal{S}}_R^z + B_L \hat{\mathcal{S}}_L^z + B_R \hat{\mathcal{S}}_R^z + H_{\mathrm{elec}} \, . \tag{1}$$

Here H_{elec} describes the effectively independent conduction electron reservoirs around each of the three QPCs, $\hat{\mathcal{S}}_{L(R)}^+$, $\hat{\mathcal{S}}_{L(R)}^-$, $\hat{\mathcal{S}}_{L(R)}^z$ are pseudospin-$\frac{1}{2}$ operators for the lowest two charge states of the left (right) islands, $\hat{s}_{L(R)}^+$ and $\hat{s}_{L(R)}^-$ are pseudospin-$\frac{1}{2}$ operators for the electronic reservoirs around the left (right) QPCs, while $c_L^{(\dagger)}$ and $c_R^{(\dagger)}$ are fermionic annihilation (creation) operators for island electrons to the left and right of the central QPC. The first line of Eq. 1 describes tunneling events at the three QPCs. The island-lead coupling terms proportional to J_L and J_R favour Kondo screening of the charge-pseudospin on the left and right islands by their attached lead, whereas the term proportional to J_C represents the pseudospin coupling between the two islands, which is correlated with electronic tunneling across the central QPC. The term proportional to I describes the inter-island capacitive interaction, while the local Zeeman pseudospin fields B_L and B_R describe the effect of plunger gates P_L and P_R. See Methods for further details of these terms.

The non-trivial physics of the model stems from the specific form of the QPC couplings J_L, J_R and J_C. The physical origin of these terms is the tunneling of spin-polarized conduction electrons onto and off the interacting islands. We obtain a description in terms of the effective charge pseudospin-$\frac{1}{2}$ operators given in Eq. 1 by projecting our model onto the reduced subspace of retained charge configurations $(N,M)/(N+1,M)/(N,M+1)/(N+1,M+1)$. For the island charge states, processes that interconvert the configurations $(N,m) \leftrightarrow (N+1,m)$ are described by the left-island charge pseudospin raising or lowering operators $\hat{\mathcal{S}}_L^\pm$, whereas processes that interconvert $(n,M) \leftrightarrow (n,M+1)$ are described by the right-island charge pseudospin operators $\hat{\mathcal{S}}_R^\pm$. In terms of the conduction electrons, $\hat{s}_L^\mp$ describes tunneling onto/off the left island from the left lead at the left QPC (Methods). Similarly, $\hat{s}_R^\pm$ corresponds to tunneling at the right QPC. $\hat{s}_{L,R}^\pm$ obey the standard spin-$\frac{1}{2}$ operator algebra, but the conventional "up" and "down" spin states usually associated with those operators are here replaced by the localization of an electron on the lead or the island, respectively. Since each tunneling event ($\hat{s}_\alpha^\pm$) must change an island's occupancy ($\hat{\mathcal{S}}_\alpha^\mp$), charge pseudospin flips necessarily accompany QPC tunneling. These island-lead couplings are the same as those for the single-island setup [19, 20, 29, 31, 32]: the correlated tunneling manifests as an anisotropic Kondo interaction. The new ingredient here is the inter-island coupling J_C. Tunneling from the right island to the left island at the central QPC via the term $c_L^\dagger c_R$ is accompanied by a simultaneous charge pseudospin flip of both islands $\hat{\mathcal{S}}_L^+ \hat{\mathcal{S}}_R^-$ since the occupation of the left island increases and the occupation of the right island decreases, $(N,M+1) \rightarrow (N+1,M)$.

The DCK model is reminiscent of the 2IK model [30], which captures the competition between Kondo screening of local moments and RKKY exchange interaction. However, the DCK model has a major difference: the inter-site coupling is not a simple exchange interaction, but rather tunneling combined with pseudospin flips on both sites (for a detailed discussion of this term, see Methods). This turns out to favour the formation of an inter-site Kondo singlet with many-body entanglement, rather than the simple two-body local spin singlet that would arise from RKKY or simple exchange. When scaled to a lattice of sites, this interaction may produce the lattice coherence effect seen in heavy fermion materials but not so far accounted for in microscopic models [24].

A crucial feature of the present charge-Kondo implementation is that the pseudospin couplings J_L, J_R and J_C are related directly to the experimental QPC transmissions of the device τ_L, τ_R and τ_C, and can be large. By tuning these couplings, one can realize various Kondo effects, and indeed a QCP, at relatively high temperatures. This contrasts with the more familiar coupling of spins between two semiconductor quantum dots, where the effective exchange interactions are perturbatively small. Furthermore, the 2IK model is an oversimplified description of real semiconductor double dot systems because it does not account for charge transfer between leads, which is known to destroy the QCP [33, 34]. Our two-island charge-Kondo system therefore presents a unique opportunity to observe a two-impurity QCP at experimentally relevant temperatures.

Results

Phase diagram and Kondo competition

The island charging energies $E_C^{L,R}$ and inter-island capacitive interaction I are finite in the physical device, so multiple island charge states play a role. This gives rise to a periodic hexagonal structure of the charge stability diagram as a function of the left and right plunger gate voltages $P_{L,R}$. We convert these to energies $U_{L,R} = U_{L,R}^0 + \alpha P_{L,R}$ using the experimentally measured capacitive lever arm $\alpha = 50$ μeV/mV, relative to an arbitrary reference $U_{L,R}^0$. $U_{L,R}$ are related to the pseudo-Zeeman fields $B_{L,R}$ in Eq. 1 via $\vec{B} = \bar{\boldsymbol{\alpha}} \vec{U}$, where $\vec{U} = (U_L, U_R)$, which accounts for cross-capacitive gate effects.

The experimental stability diagram in Fig. 1c allows us to identify regimes with particular charge states on the two

islands. In particular, we see distinct charge degeneracy lines $(N,M)/(N,M+1)$, $(N,M)/(N+1,M)$ and $(N+1,M)/(N,M+1)$, each of which is associated with single electron tunneling at one of the three QPCs (see Fig. 1b). This structure, including its characteristic gate periodicity, is reproduced very well by numerical renormalization group (NRG) [35, 36] calculations of the DCK model, generalized to take into account multiple charge-states on each island (see Methods). We fit $J_{L,R,C}$ for a given set of experimental transmissions $\tau_{L,R,C}$, as shown in Fig. 1d for the same temperature $T = 20$ mK. We note that the periodicity of the diagram extends over a larger range of gate voltages than shown (see Supplementary Information).

Along the degeneracy line $(N,M)/(N+1,M)$ the left island charge pseudospin is freely flipped by tunneling at the QPC between the left island and lead, giving rise to a Kondo effect due to the first term of Eq. 1. However, the series conductance from left to right leads through the double island structure is suppressed by this, since the conductive pathway involves virtual polarization of the Kondo singlet through the excited state $(N,M+1)$. This is supported by NRG calculations at $T = 2$ mK (Fig. 1e) which show a Kondo blockade' [37] in the series conductance as the temperature is lowered. A similar effect is seen along the degeneracy line $(N,M)/(N,M+1)$, which corresponds to a Kondo effect involving the right island and the right lead. Along the degeneracy line $(N+1,M)/(N,M+1)$, tunneling with the leads is not involved. Instead we may regard $(N+1,M)$ and $(N,M+1)$ as two components $\Leftarrow$ and $\Rightarrow$ of a collective pseudospin state of the double island structure, which is flipped by electronic tunneling at the central QPC. This gives rise to a kind of inter-island Kondo effect. The resulting Kondo singlet is disrupted by tunneling at the leads, and hence the conductance is again suppressed upon lowering the temperature. The hexagonal structure of the 2D conductance plots as a function of gate voltage for our two-site charge-Kondo system looks superficially similar to that measured for conventional semiconductor double quantum dot systems. However, the behavior in the vicinity of the triple points is very different, as shown below.

Triple point

The triple point (TP), where the $(N,M)/(N,M+1)/(N+1,M)$ charge configurations are degenerate, is a special point in the phase diagram. Here the three Kondo effects described above are all competing, see Fig. 1b. At $J_L = J_R = J_C$ in Eq. 1, the resulting frustration gives rise to a QCP, which will be the main focus of this work. By contrast, conventional semiconductor double quantum dots do not support a QCP [33, 34] (see Supplementary Information for a comparison of the two systems).

At the TP, the series conductance is enhanced because an electron can tunnel from left lead to right lead through the islands without leaving the ground state charge configurations. A crude approximation treats the QPCs as three resistors in series, and neglects electron interactions. In this case, the maximum conductance of $G = e^2/3h$ arises when the tunneling rates at each constriction are equal, $J_L = J_R = J_C$, since then there is no bottleneck in the flow of electrons through the structure. Interestingly, we observe the same maximum conductance experimentally in our device at base temperatures when the three QPCs are opened up, but here in conjunction with critical behavior (to be discussed in subsequent sections) absent in the series resistance model. This indicates strong electron interactions, and is expected from our analysis of the full DCK model: NRG calculations confirm that the conductance is indeed capped at a maximum value $G = e^2/3h$. This arises at the TP at low temperatures $T/T_K \ll 1$ when $J_L = J_R = J_C \equiv J^*$, which corresponds to the QCP. Here, we find $T_K \sim E_C \exp[-1/\nu J]$ is the Kondo temperature right at the QCP, with ν the electronic density of states at the Fermi energy (Methods). We find from NRG that the conductance $G(T)$ increases with decreasing T at the QCP, approaching the critical value as $e^2/3h - G(T) \sim (T/T_K)^{2/3}$. Opening up the QPCs (large J) boosts the Kondo temperature T_K and means that the regime of small T/T_K (and hence $G \simeq e^2/3h$) can be accessed experimentally at our base temperature of 20 mK.

We speculate that the same DCK model (and hence the same $G = e^2/3h$ maximum conductance) may be realized in a system of two coupled large semiconductor quantum dots – but only if the level spacing can be made very small ($\ll k_B T$) such that transport between QPCs through the dots is incoherent [38, 39] and if the dot states or the QPC transmissions are fully spin-polarized. However, these conditions are typically not met in conventional semiconductor double quantum dot systems, whose maximum series conductance is instead e^2/h (or $2e^2/h$ with spin degeneracy). Our observed $e^2/3h$ maximum conductance is thus already a distinctive feature of this setup.

Our theoretical analysis of the DCK model also reveals an unusual residual $T = 0$ entropy of $\Delta S = \ln(\sqrt{3})$ (Supplementary Information), establishing the QCP as a non-Fermi liquid with exotic *fractional* (anyonic) excitations. This entropic signature could in principle be observed experimentally via the techniques introduced in Refs. [40, 41]

Conductance Line Cuts

We first focus on the behavior of conductance near the TPs. Specifically, in Fig. 2a we take cuts along the line between TPs, $U_L = U_R \equiv U$, for different τ_C at fixed $\tau_L = \tau_R \equiv \tau$. $U = 0$ is chosen to be the high-symmetry point between TPs. Experimental data are compared with the corresponding NRG simulations of the device in Fig. 2b. Since every pair of triple points is indistinguishable (there are no even/odd occupancy effects in the DCK system, unlike in semiconductor double dots with spin), we extract the experimental line cuts of Fig. 2a from averages over multiple pairs of triple points.

Experiment and theory are seen to match very well in Fig. 2. At large $\tau_C > 0.7$ ($J_C > 0.4$) the positions of the split conductance peaks are captured by the theory, and at smaller τ_C (J_C) the widths of the merged conductance

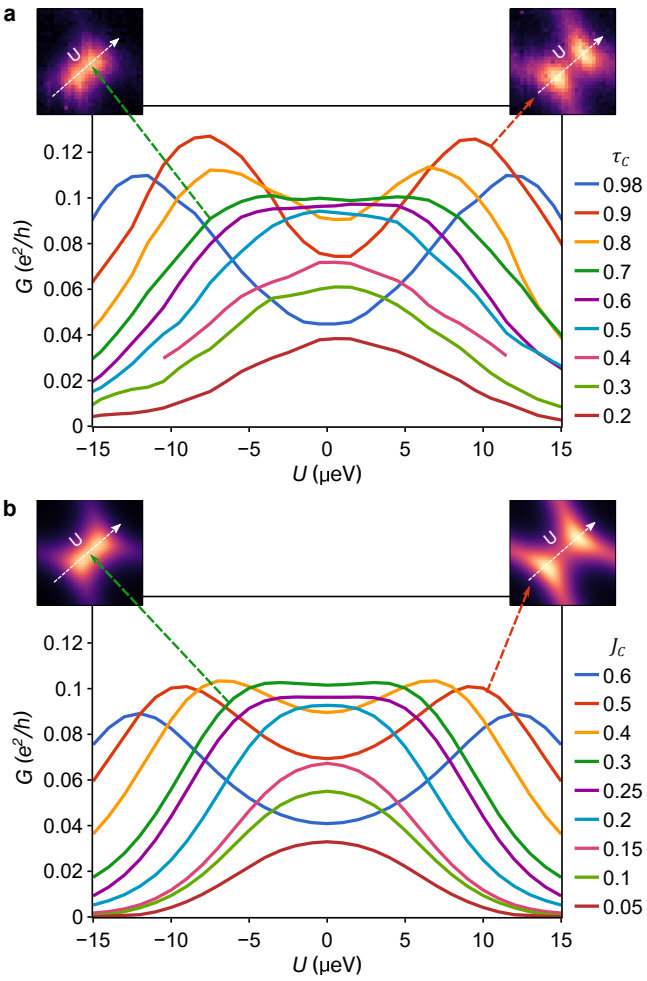

Fig. 2: Conductance line cuts between triple points. Experimentally-measured (**a**) and NRG-calculated (**b**) line cuts for $\tau = 0.38$ ($J = 0.35$ in the model) along the line $U_L = U_R \equiv U$ for different τ_C (J_C). Insets show representative 2D P_L, P_R sweeps from which line cuts are extracted. The model parameters in **b** are optimized to fit the experiment, and multiple charge states are retained for each island (Methods).

peaks are also reproduced. We note that for the largest transmissions $\tau_C \geq 0.9$, although the qualitative behavior of the experimental line cuts are still captured by NRG, the peak heights are underestimated. This is because a diverging number of island charge states [29] contribute to transport as $\tau, \tau_C \to 1$, but only a finite number of these can be retained in practice in the NRG calculations. The experimental quantum simulator can therefore provide results in this regime that are inaccessible to classical computation. Away from the limit of perfect transmission however, our results validate the DCK model as an accurate description of the physical device.

The TP positions in the space of (U_L, U_R) depend on τ_C, and at large τ_C are well separated such that they can be easily identified from the conductance peak maxima. However, even at the experimental base electron temperature of 20 mK, thermal broadening complicates the experimental analysis of the TP behavior at small τ_C, where the TPs are close together and the two conductance peaks are merged. Thus care must be taken to estimate the TP positions from the full stability diagram, and to disentangle the influence of adjacent TPs. Estimates can however be validated from NRG by going to much lower temperatures where the peaks sharpen up (compare Figs. 1d and 1e).

We see clear non-monotonicity as a function of τ_C of the maximum conductance in each line cut in Fig. 2a. This is a good indicator that the TP conductance is also non-monotonic. This is expected due to the competition between different Kondo interactions controlled by τ_C, but would not be the case for Fermi-liquid resistors in series. Taking the critical point with completely frustrated interactions to be at τ_C^* (a monotonic function of τ but not necessarily $\tau_C^* = \tau$, see Supplementary Information), we expect lower conductance for both $\tau_C > \tau_C^*$ and $\tau_C < \tau_C^*$ at low temperatures. This is because in both cases the ground state is a Fermi-liquid Kondo state, the formation of which blocks series transport across the device. The island-lead Kondo effects, which dominate for $\tau_C < \tau_C^*$, renormalize the effective QPC transmissions [19] to $\tau \to 1$ and $\tau_C \to 0$ on lowering the temperature. By contrast the inter-island Kondo effect, which dominates for $\tau_C > \tau_C^*$, renormalizes $\tau \to 0$ and $\tau_C \to 1$. Only when $\tau_C = \tau_C^*$ is the low-temperature conductance Kondo-enhanced, because in this case island-lead and inter-island Kondo singlets cannot form simultaneously (all of the renormalized QPC transmissions remain finite due to the frustration). We note that the temperature-dependence of the conductance enhancement at $\tau_C = \tau_C^*$, as well as the conductance suppression away from this point, have a non-trivial Kondo form characteristic of the QCP, the latter of which we explore next.

Despite some uncertainty in the precise TP location, the very existence of a QCP implies an underlying *universality*, in terms of which conductance signatures in its vicinity can be quantitatively analyzed.

Universal Scaling

We now turn to the behavior near the QCP, resulting from frustrated island-lead and inter-island Kondo effects. We focus on parameter regimes with large τ and τ_C, such that the corresponding critical Kondo temperatures are large. This allows experimental access to the universal regime $T/T_K \lesssim 1$. At the QCP with $\tau_C \simeq \tau_C^*$, our theoretical analysis predicts $G \simeq e^2/3h$. Moreover, non-trivial behavior is observed in the vicinity of this singular point, where perturbations drive the system away from the QCP and towards a regular Fermi liquid state. The associated conductance signatures are entirely characteristic of the quantum phase transition in this system.

Since the low-T physics near a QCP is universal and therefore insensitive to microscopic details, we use a minimal model, with only $(N, M)/(N+1, M)/(N, M+1)$ states retained in Eq. 1 (Methods). The QCP is destabilized by either detuning the couplings, corresponding to the perturbation $\Delta\tau_C = \tau_C - \tau_C^*$, or moving away from the TP via $\Delta U = U - U_{\rm TP}$ (where $U_{\rm TP}$ is the putative TP position). Remarkably, we find from NRG that any combination of $\Delta\tau_C$ and ΔU can

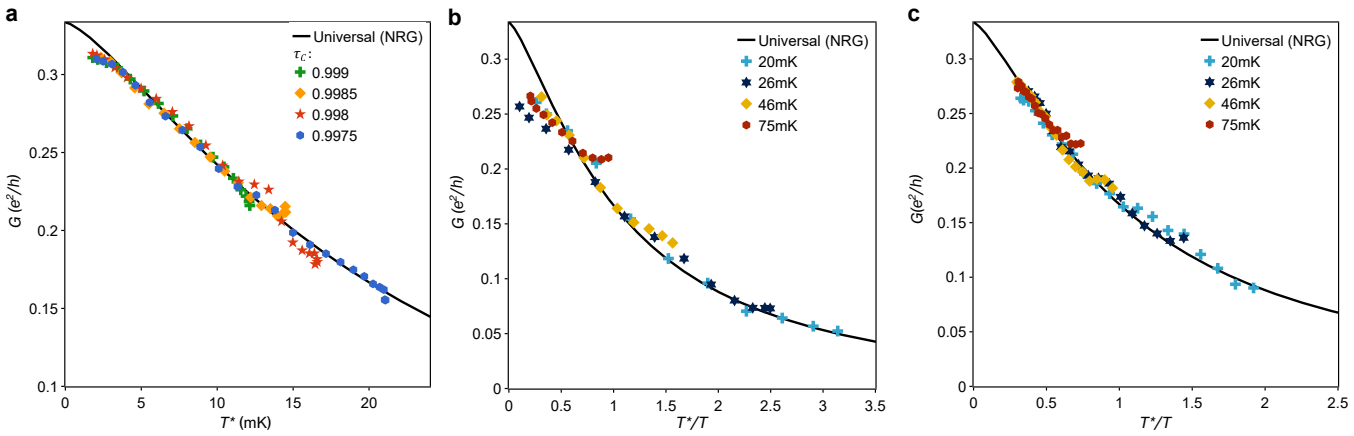

Fig. 3: Universal conductance scaling near triple point. a, Line cuts along the triple point axis, starting at a given triple point and moving away from the other. Each color/symbol corresponds to different τ_C for $\tau = 0.95$ and $T = 20$ mK. T^* is determined from Eq. 3. Since temperature is fixed, these fall on top of each other and the NRG calculated universal curve (solid line). Due to a finite detuning $\Delta\tau_C$, $T^* > 0$ even at $\Delta U = 0$. This shift and the unknown prefactor b are left as free parameters in fitting the data to the universal curve (Methods). **b,** Measured line cuts as in **a**, but at different temperatures (color/symbol) and plotted as a function of the single scaling parameter T^*/T (determined from Eq. 3) again demonstrating collapse to the universal theory curve. From lowest to highest temperatures, $\tau = \{0.78, 0.78, 0.81, 0.82\}$ and $\tau_C = 0.9$ (Methods). **c,** For the same temperature and τ, τ_C values of **b**, we now plot line cuts orthogonal to the direction of those in **b**, which also demonstrate universal scaling collapse to the same theory curve (here we use Eq. 2 to determine T^*/T). Further analysis is provided in Supplementary Information.

be captured by a *single* Fermi-liquid scale T^* characterizing the flow away from the QCP toward a Fermi-liquid state, provided the magnitude of the perturbations is small:

$$T^* = a|\Delta\tau_C|^{3/2} + b|\Delta U|^{3/2} \tag{2}$$

with a, b constants. We expect universal behavior of the system as a function of T^*/T when $T^* \ll T_K$. When $T^*/T \gg 1$, the system is firmly within a Fermi-liquid regime, and in the opposite limit the system is near the QCP. From NRG we can calculate the universal conductance crossover as a function of T^*/T in the close vicinity of a TP. This is shown as the solid lines in Fig. 3 and has asymptotic behavior $e^2/3h - G(T) \sim (T^*/T)^{4/3}$ for $T^*/T \ll 1$ and $G(T) \sim (T^*/T)^{-2}$ for $T^*/T \gg 1$ (see also Supplementary Information).

However, since Eq. 2 is calculated with the minimal DCK model where each island is restricted to two charge states, it cannot capture the full behavior of our experiment. The DCK model contains a single pair of TPs, whereas the charge stability diagrams of Fig. 1 exhibit a periodicity in gate voltage space and feature repeated TP pairs. In particular, starting at one TP and then increasing ΔU, we must eventually encounter another TP. This implies a periodicity in the Fermi liquid scale T^* that is not captured by the universal result Eq. 2, which holds only for small values of the perturbation. Phenomenologically, the simplest form to correctly capture the observed periodicity, while also reducing to the known behavior of Eq. 2 in the close vicinity of any given TP, is:

$$T^* = a|\Delta\tau_C|^{3/2} + b|\cos(2\pi U/\delta) - \Delta_{TP}|^{3/2} \tag{3}$$

Here, δ is the spacing between pairs of triple points and Δ_{TP} is related to the splitting of the two triple points in a given pair, such that $\Delta_{TP} = \cos(2\pi U_{\mathrm{TP}}/\delta)$. We define $U = 0$ as being halfway between a pair of TPs, as in Fig. 2. In fact, this periodic form of T^* was recently proved as an exact result in the large τ, τ_C limit [42]. Remarkably then, we can extend the notion of universality in this system to include the periodic behavior seen over much larger ranges of gate voltage. Conductance data of our device configured to different τ, τ_C, U, and T should collapse to the same universal curve when rescaled in terms of T^*/T. Since the universal curve only depends on the single scaling parameter T^*/T, it can be obtained by NRG for the DCK model (even though these calculations are in practice done in the opposite limit τ, $\tau_C \ll 1$).

To confirm this experimentally, we must first identify the TP position ($\Delta U = 0$), since this determines Δ_{TP}. This is relatively straightforward when the TPs are well separated, which occurs when τ_C is large, and we simply take U_{TP} as the peak position. The overall gate periodicity δ is also easily extracted from the experimental charge stability diagram. We then determine T^* from Eq. 3 using U and τ_C from line cuts similar to those of Fig. 2a for fixed $\tau = 0.95$ and $T = 20$ mK. The experimental data (symbols) collapse to the NRG universal curve (line), as shown in Fig. 3a, revealing the non-trivial $3/2$ power law scaling in the data (see Supplementary Information for further analysis). The generalized periodic form of T^* in Eq. 3 is expected to hold here since τ and τ_C are both large. Note that $\Delta\tau_C$ here is not in general zero, but the additive form of the contributions to T^* from different perturbations means that any such detuning in τ_C generates a finite T^* even when $\Delta U = 0$. We account for this by a simple shift when plotting the data in terms of T^*. The deviation from the universal curve at low T^* is attributed to a finite T/T_K, which simply means that the quantum critical

state is not fully developed at experimental base temperatures even when $T^* = 0$.

We confirm the universality in Fig. 3b by measuring and rescaling line cuts at different temperatures. Plotting the data as a function of the universal parameter T^*/T yields good data collapse to the universal theory curve. At each temperature, τ and τ_C are adjusted such that the conductance at $\Delta U = 0$ is roughly the same (we use somewhat smaller values of τ and τ_C than in Fig. 3a). We do not expect to satisfy $\tau_C = \tau_C^*$ for each set. Identifying the TP position is more complicated at higher temperatures as thermal broadening smears the peaks, so we extract δ and Δ_{TP} at 20 mK, and use the same values at higher temperatures (Methods).

The scaling collapse as a function of T^*/T and strong quantitative agreement with the non-trivial universal conductance curve obtained by theory is both striking and a direct signature of the critical point. Significantly, the collapse is over the entire range of T^*/T for each line cut, with limitations only at small T^*/T due to the finite T/T_K mentioned previously. We attribute the breakdown in scaling for the data collected at the highest temperature of 75 mK to be due to a breakdown of the assumption $k_B T \ll E_C$, on which the derivation of the DCK model relies.

In the case of the data presented in Fig. 3b, we comment that the limit of large τ, τ_C is in fact not well satisfied. The use of Eq. 3 here is reasonable but only conjecture. However, our experimental results do suggest that Eq. 3 holds more generally. This illustrates the power of quantum simulation to obtain results beyond reach of other methods.

While most of this work has focused on line cuts along the axis connecting triple points ($U_L = U_R$), in fact Eq. 2 holds for gate detuning ΔU away from the TP in any direction in the space of (U_L, U_R). In Fig. 3c we present line cut data along the orthogonal direction, parallel to $U_L = -U_R$, for the same couplings as plotted in Fig. 3b. The periodic structure of the charge stability diagram is different along these cuts and so we cannot use Eq. 3 (no simple form is known from theory). However the effect of neighboring TPs and higher charge states is less pronounced as ΔU is increased in this direction, and so the simpler form of Eq. 2 is quite sufficient in practice. We again see excellent data collapse to the universal theory curve at all temperatures considered (and now even the 75 mK data). This further strengthens the sense of universality in this system, since the same behavior is observed by perturbing the QCP in different directions around the TP – an emergent isotropy in gate space not present in the bare model.

Discussion

In this work, we have presented strong evidence for a quantum phase transition in a two-site circuit. By exploiting the charge-Kondo paradigm, our device maps to a variant of the celebrated two-impurity Kondo model, here featuring a phase in which the local moments on the two islands are screened *collectively* by many-body effects driven by conduction electron scattering. This may have relevance for the emergence of lattice coherence in Kondo lattice systems.

We formulate a model to describe the two-island charge-Kondo device, and demonstrate quantitative agreement between NRG calculations and experimentally measured conductance, including in the universal regime of the exotic quantum critical point.

Our work on the crucial role of the inter-island interaction paves the way for a host of other studies. Opening each of the islands to a second lead (already present but not used in the existing device) would produce two sites each hosting a two-channel Kondo (2CK) state at low temperatures [19]. Our existing device allows the coupling between two such 2CK states to be studied. Alternatively, by preparing a single 2CK state on one island, the associated Majorana zero mode localized on that island [43, 44] could conceivably be transferred to the other island by gate voltage tuning. This could eventually allow for the manipulation and even braiding of anyonic excitations arising from Kondo interactions in nanoelectronic circuits.

Unlike for tunnel-coupled semiconductor quantum dots, there is no clear roadblock to scaling this platform to more complex uniform clusters of coupled charge-Kondo islands, and ultimately lattices. This provides a way of examining with unprecedented control some of the most subtle collective dynamics of real correlated materials, and introducing a flexible set of effective interactions. Such scaled-up charge-Kondo clusters would act as analog quantum simulators with capabilities beyond classical computation: three coupled islands is already out of reach for NRG, while stochastic algorithms such as Quantum Monte Carlo (QMC) [6] may not be able to access the universal low-temperature dynamics of these systems. Indeed, tunable analog quantum simulators of this type may eventually form the basis for calculations requiring solutions of complex cluster models that are difficult to obtain using NRG or even QMC, as arise for example as inputs to extensions of dynamical mean field theory (DMFT) [45, 46] for correlated materials such as the high-temperature superconductors.

Acknowledgements

We thank F. Pierre, I. Safi, G. Zarand, C.P. Moca, I. Weymann, P. Sriram, E. Sela, Y. Oreg, Q. Si, C. Varma, and C. Mora for their scientific insights and suggestions. To make this project work, before coupling two islands we had to start by reproducing F. Pierre's tour de force experiments on single islands of the same type. F. Pierre helped with comments on our fabrication process, measurement procedure, and analysis. Discussions with C. Mora led to improvements in our analysis of the periodic Fermi liquid scale. We acknowledge G. Zarand, C.P. Moca, and I. Weymann for early discussions of the Hamiltonian and its implications. Measurement and analysis were supported by the U.S. Department of Energy (DOE), Office of Science, Basic Energy Sciences (BES), under Contract DE-AC02-76SF00515. Growth and characterization of heterostructures was supported by the French Renatech network. Theory and computation (A.K.M.) were supported by the Irish Research Council Laureate Awards 2017/2018

through Grant No. IRCLA/2017/169. Part of this work was performed at the Stanford Nano Shared Facilities (SNSF), supported by the National Science Foundation under award ECCS-2026822. Early research that established how to meet the demanding technical conditions for sample fabrication and basic measurements was supported by the National Science Foundation (NSF) under award no. 1608962. W.P. acknowledges support from the Fletcher Jones Fellowship. C.L.H. acknowledges support from the Gabilan Fellowship. L.P. acknowledges support of the Albion Walter Hewlett Fellowship.

Author Contributions

W.P. and L.P. performed the measurements. L.P. fabricated the device. A.K.M. developed the theory and did NRG calculations. W.P., L.P., C.L.H., M.A.K., A.K.M., and D.G.-G. analyzed the data. A.C. and U.G. grew the heterostructure that hosts the 2DEG on which these samples are built. D.G.-G. supervised the project.

Competing Financial Interests

The authors declare no competing financial interests.

References

[1] Sachdev, S. *Quantum Phase Transitions* (Cambridge University Press, 2011), 2 edn.

[2] Paschen, S. & Si, Q. Quantum phases driven by strong correlations. *Nat Rev Phys* **3**, 9–26 (2021).

[3] Anderson, P. W. Localized magnetic states in metals. *Phys. Rev.* **124**, 41–53 (1961).

[4] Georges, A. & Sengupta, A. M. Solution of the Two-Impurity, Two-Channel Kondo Model. *Phys. Rev. Lett.* **74**, 2808–2811 (1995).

[5] Affleck, I. Quantum impurity problems in condensed matter physics (2008).

[6] Gull, E. *et al.* Continuous-time Monte Carlo methods for quantum impurity models. *Rev. Mod. Phys.* **83**, 349–404 (2011).

[7] Meirav, U., Kastner, M. A. & Wind, S. J. Single-electron charging and periodic conductance resonances in GaAs nanostructures. *Phys. Rev. Lett.* **65**, 771–774 (1990).

[8] Goldhaber-Gordon, D. *et al.* Kondo effect in a single-electron transistor. *Nature* **391**, 156–159 (1998).

[9] Cronenwett, S. M., Oosterkamp, T. H. & Kouwenhoven, L. A Tunable Kondo Effect in Quantum Dots. *Science* **281**, 540–544 (1998).

[10] Sasaki, S. *et al.* Kondo effect in an integer-spin quantum dot. *Nature* **405**, 764–767 (2000).

[11] Jeong, H., Chang, A. M. & Melloch, M. R. The Kondo effect in an artificial quantum dot molecule. *Science* **293**, 2221–2223 (2001).

[12] Oreg, Y. & Goldhaber-Gordon, D. Two-Channel Kondo Effect in a Modified Single Electron Transistor. *Phys. Rev. Lett.* **90**, 136602 (2003).

[13] Potok, R. M., Rau, I. G., Shtrikman, H., Oreg, Y. & Goldhaber-Gordon, D. Observation of the two-channel Kondo effect. *Nature* **446**, 167–171 (2007).

[14] Buizert, C., Oiwa, A., Shibata, K., Hirakawa, K. & Tarucha, S. Kondo Universal Scaling for a Quantum Dot Coupled to Superconducting Leads. *Phys. Rev. Lett.* **99**, 136806 (2007).

[15] Takada, S. *et al.* Transmission Phase in the Kondo Regime Revealed in a Two-Path Interferometer. *Phys. Rev. Lett.* **113**, 126601 (2014).

[16] Keller, A. J. *et al.* Emergent SU(4) Kondo physics in a spin–charge-entangled double quantum dot. *Nature Phys* **10**, 145–150 (2013).

[17] Mitchell, A. K., Liberman, A., Sela, E. & Affleck, I. SO(5) Non-Fermi Liquid in a Coulomb Box Device. *Phys. Rev. Lett.* **126**, 147702 (2021).

[18] Keller, A. J. *et al.* Universal Fermi liquid crossover and quantum criticality in a mesoscopic system. *Nature* **526**, 237–40 (2015).

[19] Iftikhar, Z. *et al.* Two-channel Kondo effect and renormalization flow with macroscopic quantum charge states. *Nature* **526**, 233–236 (2015).

[20] Iftikhar, Z. *et al.* Tunable quantum criticality and super-ballistic transport in a "charge" Kondo circuit. *Science* **360**, 1315–1320 (2018).

[21] Landau, L. A., Cornfeld, E. & Sela, E. Charge Fractionalization in the Two-Channel Kondo Effect. *Phys. Rev. Lett.* **120**, 186801 (2018).

[22] Mitchell, A. K., Landau, L. A., Fritz, L. & Sela, E. Universality and Scaling in a Charge Two-Channel Kondo Device. *Phys. Rev. Lett.* **116**, 157202 (2016).

[23] Zhang, G. *et al.* Nonequilibrium quantum critical steady state: Transport through a dissipative resonant level. *Phys. Rev. Research* **3**, 013136 (2021).

[24] Burdin, S., Georges, A. & Grempel, D. R. Coherence Scale of the Kondo Lattice. *Phys. Rev. Lett.* **85**, 1048–1051 (2000).

[25] Stafford, C. A. & Das Sarma, S. Collective coulomb blockade in an array of quantum dots: A mott-hubbard approach. *Phys. Rev. Lett.* **72**, 3590–3593 (1994).

[26] Hensgens, T. *et al.* Quantum simulation of a Fermi-Hubbard model using a semiconductor quantum dot array. *Nature* **548**, 70–73 (2017).

[27] Pateras, A. *et al.* Electrode-induced lattice distortions in gaas multi-quantum-dot arrays. *Journal of Materials Research* **34**, 1291–1301 (2019).

[28] Inoshita, T., Shimizu, A., Kuramoto, Y. & Sakaki, H. Correlated electron transport through a quantum dot: The multiple-level effect. *Phys. Rev. B* **48**, 14725–14728 (1993).

[29] Furusaki, A. & Matveev, K. Theory of strong inelastic cotunneling. *Physical Review B* **52**, 16676 (1995).

[30] Jones, B. A., Varma, C. M. & Wilkins, J. W. Low-Temperature Properties of the Two-Impurity Kondo Hamiltonian. *Phys. Rev. Lett.* **61**, 125–128 (1988).

[31] Glazman, L. & Matveev, K. Lifting of the coulomb blockade of one-electron tunneling by quantum fluctuations. *Sov. Phys. JETP* **71**, 1031–1037 (1990).

[32] Matveev, K. A. Quantum fluctuations of the charge of a metal particle under the Coulomb blockade conditions. *Sov. Phys. JETP* **72**, 892–899 (1991).

[33] Zaránd, G., Chung, C.-H., Simon, P. & Vojta, M. Quantum Criticality in a Double-Quantum-Dot System. *Phys. Rev. Lett.* **97**, 166802 (2006).

[34] Jayatilaka, F. W., Galpin, M. R. & Logan, D. E. Two-channel Kondo physics in tunnel-coupled double quantum dots. *Phys. Rev. B* **84**, 115111 (2011).

[35] Bulla, R., Costi, T. A. & Pruschke, T. Numerical renormalization group method for quantum impurity systems. *Rev. Mod. Phys.* **80**, 395–450 (2008).

[36] Mitchell, A. K., Galpin, M. R., Wilson-Fletcher, S., Logan, D. E. & Bulla, R. Generalized Wilson chain for solving multichannel quantum impurity problems. *Phys. Rev. B* **89**, 121105 (2014).

[37] Mitchell, A. K., Pedersen, K. G., Hedegård, P. & Paaske, J. Kondo blockade due to quantum interference in single-molecule junctions. *Nat Commun.* **8**, 1–10 (2017).

[38] Averin, D. & Odintsov, A. Macroscopic quantum tunneling of the electric charge in small tunnel junctions. *Physics Letters A* **140**, 251–257 (1989).

[39] Averin, D. & Nazarov, Y. V. Virtual electron diffusion during quantum tunneling of the electric charge. *Physical Review Letters* **65**, 2446 (1990).

[40] Child, T. *et al.* Entropy measurement of a strongly correlated quantum dot. *arXiv preprint arXiv:2110.14158* (2021).

[41] Han, C. *et al.* Fractional entropy of multichannel kondo systems from conductance-charge relations. *Physical Review Letters* **128**, 146803 (2022).

[42] Karki, D. B., Boulat, E. & Mora, C. Double-charge quantum island in the quasiballistic regime. *Phys. Rev. B* **105**, 245418 (2022).

[43] Emery, V. J. & Kivelson, S. Mapping of the two-channel Kondo problem to a resonant-level model. *Phys. Rev. B* **46**, 10812–10817 (1992).

[44] Coleman, P., Ioffe, L. B. & Tsvelik, A. M. Simple formulation of the two-channel Kondo model. *Phys. Rev. B* **52**, 6611–6627 (1995).

[45] Maier, T. The Dynamical Cluster Approximation and its DCA+ Extension . In Pavarini, E., Koch, E. & Coleman, P. (eds.) *Many-Body Physics: From Kondo to Hubbard*, vol. 5, chap. 14 (Forschungszentrum Jülich, 2015).

[46] Sénéchal, D. Quantum Cluster Methods: CPT and CDMFT. In Pavarini, E., Koch, E. & Coleman, P. (eds.) *Many-Body Physics: From Kondo to Hubbard*, vol. 5, chap. 13 (Forschungszentrum Jülich, 2015).

METHODS

Theoretical Modeling of the Device

Here we provide further details of our theoretical modeling of the two-site device leading to the DCK model, Eq. 1 – see Extended Data Fig. 1. We also discuss the multiple charge-state generalization and the minimal triple point model. Further details can be found in the Supplementary Information.

The conduction electrons in the DCK system live in six reservoirs in total, one on each side of each of the three QPCs: one on the left lead, two on each island, and one on the right lead. We treat the electrons on the islands as forming an effective continuum because their level spacing $\delta \ll k_B T$ even at the experimental base temperature $T = 20$ mK. Reservoirs denoted $f_{\alpha i}$ and c_α of island $\alpha = L, R$ are treated within the model as being independent because of the metal component separating them. Physically, electrons can diffuse across each island through the metal component, but this intra-island transport between QPCs is incoherent precisely because $\delta \ll k_B T$ [38, 39]. Following Ref. [29], we neglect this incoherent transport, and model $f_{\alpha i}$ and c_α in each island as distinct electronic continua in the thermodynamic limit. The physics is insensitive to the precise number of electrons in these reservoirs since this number is very large. Electrons in lead $\alpha = L, R$ are denoted $f_{\alpha l}$. See Extended Data Fig. 1a for a schematic of the setup. The free conduction electrons are described by $H_{\rm elec}$ in Eq. 1, given by,

$$H_{\rm elec} = \sum_{\alpha,\gamma,k} \epsilon_k f^\dagger_{\alpha\gamma k} f_{\alpha\gamma k} + \sum_{\alpha,k} \epsilon_k c^\dagger_{\alpha k} c_{\alpha k} \ , \tag{4}$$

where $\alpha = L, R$ (for left or right) and $\gamma = l, i$ (for lead or island). The dispersion ϵ_k describes the single-particle energy of an electron with momentum k (all reservoirs are assumed equivalent for simplicity, but this is inconsequential); we take the density of states to be constant, $\nu = 1/2D$, inside a band of half-width D.

Electronic tunneling at the QPCs is described by,

$$H_{\rm QPC} = \sum_{\alpha=L,R} J_\alpha \left(f^\dagger_{\alpha l} f_{\alpha i} + \text{H.c.} \right) + J_C \left(c^\dagger_L c_R + \text{H.c.} \right) \ , \tag{5}$$

where the localized orbitals at the QPC positions are defined as $f_{\alpha\gamma} = \sum_k \zeta_k f_{\alpha\gamma k}$ and $c_\alpha = \sum_k \zeta_k c_{\alpha k}$, with expansion coefficients ζ_k. Tunneling events at the QPCs described by $H_{\rm QPC}$ change the charge-state configurations (n, m) of the islands (here n (m) is the number of electrons on the left (right) island). We denote the corresponding macroscopic charge states of the islands as $|n, m\rangle$, such that the number operators for the left and right islands are given by,

$$\begin{aligned} \hat{N}_L &= \textstyle\sum_{n,m} \ n|n,m\rangle\langle n,m| \ , \\ \hat{N}_R &= \textstyle\sum_{n,m} \ m|n,m\rangle\langle n,m| \ . \end{aligned}$$

The island occupancies are then changed by ladder operators,

$$\begin{aligned} \hat{N}^\pm_L &= \textstyle\sum_{n,m} \ |n \pm 1, m\rangle\langle n,m| \ , \\ \hat{N}^\pm_R &= \textstyle\sum_{n,m} \ |n, m \pm 1\rangle\langle n,m| \ . \end{aligned}$$

See Supplementary Information for more details.

Using these operators, we describe the effect of the gate-controlled local potentials as,

$$H_{\rm gate} = B_L \hat{N}_L + B_R \hat{N}_R \ , \tag{6}$$

and the effect of electronic interactions as,

$$H_{\rm int} = E^L_C \hat{N}^2_L + E^R_C \hat{N}^2_R + I \hat{N}_L \hat{N}_R \ . \tag{7}$$

The full microscopic Hamiltonian then follows as $H = H_{\rm elec} + H_{\rm QPC} + H_{\rm gate} + H_{\rm int}$.

To obtain an effective charge-Kondo model from H, we make two simple and well-controlled approximations – both of which follow from the original charge-Kondo proposals of Matveev and coworkers [31, 32]. First, we relax the exact constraints that $\hat{N}_\alpha = \sum_k f^\dagger_{\alpha i k} f_{\alpha i k} + \sum_k c^\dagger_{\alpha k} c_{\alpha k}$, and promote $\hat{N}_L$ and $\hat{N}_R$ to independent quantum degrees of freedom. This is a good approximation when the islands host a very large number of electrons in a quasi-continuum, since the *dynamics* of $\hat{N}_L$ and $\hat{N}_R$ should in this limit be unaffected by the precise number of electrons on the islands (that is, the physics is controlled by *changes* in the occupations rather than the occupations themselves). This limit is well satisfied in practice by the experimental setup. In this case we replace $f_{\alpha i k} \to f_{\alpha i k} \hat{N}^-_\alpha$ and $c_{\alpha k} \to c_{\alpha k} \hat{N}^-_\alpha$. The second approximation is to project the the full Hamiltonian H onto a reduced subspace of thermally accessible island charge configurations to obtain an effective model $H_{\rm eff} = \hat{P} \hat{H} \hat{P}$. This is a valid approximation at low temperatures $k_B T \ll E^{L,R}_C$ provided the QPCs are not opened up (a macroscopic number of charge states are involved near perfect transmission [29], so we additionally require $\nu J_{L,C,R} \ll 1$ for the projection step).

DCK Model: The DCK model, Eq. 1, is obtained (up to an irrelevant constant) by following the above steps, when we retain only the charge configurations (n, m) with $n = N$ or $N + 1$ and $m = M$ or $M + 1$. That is, $H_{\rm DCK} = \hat{P} \hat{H} \hat{P}$ with the projector,

$$\begin{aligned} \hat{P} \ &= \ |N,M\rangle\langle N,M| + |N+1,M+1\rangle\langle N+1,M+1| \\ &+ \ |N+1,M\rangle\langle N+1,M| + |N,M+1\rangle\langle N,M+1| \ . \end{aligned}$$

We now introduce pseudospin-$\frac{1}{2}$ raising/lowering operators to describe transitions between the two retained charge states of each island,

$$\begin{aligned} \hat{\mathcal{S}}^+_L &= \textstyle\sum_{m=M}^{M+1} \ |N+1,m\rangle\langle N,m| \ , \\ \hat{\mathcal{S}}^+_R &= \textstyle\sum_{n=N}^{N+1} \ |n,M+1\rangle\langle n,M| \ , \end{aligned}$$

and with $\hat{\mathcal{S}}^-_\alpha = (\hat{\mathcal{S}}^+_\alpha)^\dagger$. We also define,

$$\begin{aligned} \hat{\mathcal{S}}^z_L &= \textstyle\sum_{m=M}^{M+1} \ \frac{1}{2}[|N+1,m\rangle\langle N+1,m| - |N,m\rangle\langle N,m|] \ , \\ \hat{\mathcal{S}}^z_R &= \textstyle\sum_{n=N}^{N+1} \ \frac{1}{2}[|n,M+1\rangle\langle n,M+1| - |n,M\rangle\langle n,M|] \ . \end{aligned}$$

The effective DCK model then reads,

$$\begin{aligned} H_{\rm DCK} = \Big(& J_L \hat{\mathcal{S}}^+_L f^\dagger_{Li} f_{Ll} + J_R \hat{\mathcal{S}}^+_R f^\dagger_{Ri} f_{Rl} \\ & + J_C \hat{\mathcal{S}}^+_L \hat{\mathcal{S}}^-_R c^\dagger_L c_R + \text{H.c.} \Big) \\ & + I \hat{\mathcal{S}}^z_L \hat{\mathcal{S}}^z_R + B_L \hat{\mathcal{S}}^z_L + B_R \hat{\mathcal{S}}^z_R + H_{\rm elec} \ . \end{aligned} \tag{8}$$

We obtain Eq. 1 by further defining the pseudospin-$\frac{1}{2}$ operators $\hat{s}^-_\alpha = f^\dagger_{\alpha i} f_{\alpha l}$ and $\hat{s}^+_\alpha = (\hat{s}^-_\alpha)^\dagger$.

Minimal Model at TP: At the TP, we can further project the model onto the restricted three-dimensional subspace of charge configurations $|A\rangle = |N, M\rangle$, $|B\rangle = |N+1, M\rangle$ and $|C\rangle = |N, M+1\rangle$ using the projector $\hat{P} = \sum_{\xi=A,B,C} |\xi\rangle\langle\xi|$. This leads to a minimal model valid close to the TP,

$$H_{\rm TP} = \big(J_L \hat{s}^-_L |B\rangle\langle A| + J_C \hat{s}^-_C |C\rangle\langle B| + J_R \hat{s}^-_R |A\rangle\langle C| + \text{H.c.}\big) + H_{\rm leads} + H_{\rm gate} \ , \tag{9}$$

where we have additionally defined $\hat{s}^-_c = c^\dagger_R c_L$, and $H_{\rm gate} = \sum_{\xi=A,B,C} \Delta U_\xi |\xi\rangle\langle\xi|$ describes gate-voltage detuning away from the TP. The QCP is realized by setting $J_L = J_C = J_R \equiv J$ and $H_{\rm gate} = 0$ in Eq. 9, and is illustrated schematically in Extended Data Fig. 1b. Finite $H_{\rm gate}$ then generates a Fermi liquid crossover on the scale of T^* as discussed in the main text. Eq. 9 is solved by NRG and used to obtain the universal conductance curves near the TP shown in Fig. 3, and to extract numerically the dependence of T_K on J as mentioned in the main text.

At the QCP of the DCK model, enhanced series conductance between leads proceeds via the following mechanism (see blue arrows in Extended Data Fig. 1b). We start from the charge configuration $|A\rangle = |N, M\rangle$. First, an electron tunnels from the left lead (f_{Ll}) onto the left side of the left island ($f^\dagger_{Li}$), thus flipping the left island charge pseudospin from "down" to "up" ($\mathcal{S}^+_L$, meaning $N \to N+1$). This converts $|A\rangle \to |B\rangle$. In the second step, an electron tunnels from the right side of the left island (c_L) at the central QPC to the left side of the right island ($c^\dagger_R$). This simultaneously lowers the charge pseudospin of the left island back to "down" and raises the charge pseudospin of the right island to "up" ($\mathcal{S}^-_L \mathcal{S}^+_R$, meaning $N+1 \to N$ and $M \to M+1$). This step converts $|B\rangle \to |C\rangle$. In the final step, an electron tunnels from the right side of the right island (f_{Ri}) onto the right lead ($f^\dagger_{Rl}$), which also flips the charge pseudospin on the right island back to "down" ($\mathcal{S}^-_R$, meaning $M+1 \to M$). Overall an electron is transferred from the left lead to the right lead, but the device charge configuration has been "reset", $|C\rangle \to |A\rangle$, ready for transfer of the next electron. In the DCK model, U(1) charge is separately conserved in each of the three 'channels' f_{Ll}/f_{Li}, f_{Rl}/f_{Ri}, and c_L/c_R (whereas only a global U(1) symmetry applies in the physical device). The transport mechanism described above leaves an extra electron in f_{Li} and c_R and an extra hole in c_L and f_{Ri}. Overall charge conservation is still maintained, as this is enforced by the charge pseudospin dynamics of $\boldsymbol{\mathcal{S}}_L$ and $\boldsymbol{\mathcal{S}}_R$. The generation of particle-hole pairs in the island reservoirs is irrelevant for the pseudospin dynamics because the island reservoirs are treated as electronic continua in the thermodynamic limit, and calculations are performed in the grand canonical ensemble.

Generalized Multi-Level DCK Model: To capture the periodicity in the experimental charge stability diagram (Fig. 1c) and to relax the constraints $k_B T \ll E_C^{L,R}$ and $\nu J_{L,C,R} \ll 1$, we can include more than just two charge states of each island in our projection to the effective model. This is important for making quantitative comparisons with the experimental results in Figs. 1 and 2. In particular, the experiment is not confined to small pseudospin coupling.

The generalized DCK model $H_{\rm gen} = \hat{P} H \hat{P}$ is obtained using the projector

$$\hat{P} \ = \ \sum_{n=N-\bar{N}}^{N+\bar{N}+1} \ \sum_{m=M-\bar{M}}^{M+\bar{M}+1} \ |n;m\rangle\langle n;m| \ .$$

Here N and M are reference fillings, while $\bar{N}$ and $\bar{M}$ determine the number of included island charge states. Up to irrelevant constants, the result of the projection is,

$$\begin{aligned} H_{\rm gen} = \Big(&J_L \hat{\mathbb{S}}^+_L \hat{s}^-_L + J_R \hat{\mathbb{S}}^+_R \hat{s}^-_R + J_C \hat{\mathbb{S}}^+_L \hat{\mathbb{S}}^-_R c^\dagger_L c_R + \text{H.c.}\Big) \\ &+ E_C^L (\hat{N}_L - N - \tfrac{1}{2})^2 + E_C^R (\hat{N}_R - M - \tfrac{1}{2})^2 \\ &+ I (\hat{N}_L - N - \tfrac{1}{2})(\hat{N}_R - M - \tfrac{1}{2}) \\ &+ B_L \hat{N}_L + B_R \hat{N}_R + H_{\rm elec} \ , \end{aligned} \tag{10}$$

where now we have:

$$\begin{aligned} \hat{\mathbb{S}}^+_L \ &= \ \sum_{n=N-\bar{N}}^{N+\bar{N}} \ \sum_{m=M-\bar{M}}^{M+\bar{M}+1} \ |n+1,m\rangle\langle n,m| \ , \\ \hat{\mathbb{S}}^+_R \ &= \ \sum_{n=N-\bar{N}}^{N+\bar{N}+1} \ \sum_{m=M-\bar{M}}^{M+\bar{M}} \ |n,m+1\rangle\langle n,m| \ , \end{aligned}$$

and with $\hat{\mathbb{S}}^-_\alpha = (\hat{\mathbb{S}}^+_\alpha)^\dagger$.

Eq. 10 reduces to the DCK model Eq. 1 for $\bar{N} = \bar{M} = 0$ when only two charge states are accessible per island. By contrast, the effect of the projection is entirely removed by taking the formal limit $N, \bar{N}, M, \bar{M} \to \infty$. The generalized model therefore allows to interpolate between these limiting cases by tuning $\bar{N}$ and $\bar{M}$. Although a relatively small number of charge states can be retained for numerical calculations in practice (see below for details), one can check *post hoc* that results are converged with respect to increasing $\bar{N}$ and $\bar{M}$ for a given set of physical model parameters.

NRG calculations

To simulate the experimental two-island charge-Kondo device using NRG [35, 47], we employ the effective models developed above. Universal results near the critical TP presented in Fig. 3 of the main text were obtained by NRG using Eq. 9. Figs. 1 and 2 feature NRG results using the generalized multi-level model Eq. 10, which allows to capture the full phase diagram and gate-voltage periodicity.

NRG involves discretizing the conduction electron Hamiltonian $H_{\rm elec}$ logarithmically, mapping to semi-infinite tight-binding Wilson chains, and diagonalizing the discretized model iteratively. N_s of the lowest energy states are retained at each step, resulting in an RG procedure which reveals the physics on progressively lower energy scales [35, 47].

Standard NRG cannot be used in our case, however, due to the complexity of the models at hand, with 6 spinless conduction electron channels. Instead, we use the 'interleaved NRG' (iNRG) method [36, 48], which involves mapping $H_{\rm elec}$ to a single generalized Wilson chain. This dramatically lowers the computational cost of such calculations, and brings the numerical solution of the models within reach. For all iNRG calculations presented in this work, we use a logarithmic

discretization parameter $\Lambda = 4$, retain $N_s = 35000$ states at each iteration, and exploit all abelian quantum numbers. When using the generalized model Eq. 10 we used $\bar{N} = \bar{M} = 7$, corresponding to 16 retained charge states per island. By contrast, the universal critical physics of the TP can be obtained from Eq. 9, retaining just 3 charge states for the entire two-site system.

The experimental quantity of interest is the series dc linear response differential conductance,

$$G = \left.\frac{dI}{dV_b}\right|_{V_b \to 0} \tag{11}$$

where we take $I = -e\langle \dot{N}_{Rl} \rangle$ to be the current into the right lead due to a voltage V_b applied to the left lead. Here $\dot{N}_{Rl} = \frac{d}{dt}\hat{N}_{Rl}$ and $\hat{N}_{\alpha l} = \sum_k f^\dagger_{\alpha lk} f_{\alpha lk}$. An ac voltage bias on the left lead can be incorporated by a source term in the Hamiltonian, $H_{\rm bias} = -eV_b \cos(\omega t)\hat{N}_{Ll}$, where ω is the ac driving frequency. The dc limit is obtained as $\omega \to 0$.

The geometry of the device means that the conductance cannot be related to a spectral function. Instead we use the Kubo formula [49],

$$G = \frac{e^2}{h} \lim_{\omega \to 0} \frac{-2\pi \ {\rm Im}K(\omega)}{\omega} \ , \tag{12}$$

where $K(\omega) = \langle\langle \dot{N}_{Ll}; \dot{N}_{Rl} \rangle\rangle$ is the Fourier transform of the retarded current-current correlator $K(t) = -i\theta(t)\langle [\dot{N}_{Ll}, \dot{N}_{Rl}(t)] \rangle$. Within iNRG, ${\rm Im}K(\omega)$ may be obtained from its Lehmann representation using the full density matrix technique [50]. The numerical evaluation is substantially improved by utilizing the identity ${\rm Im}K(\omega) = \omega^2 {\rm Im}\langle\langle \hat{N}_{Ll}; \hat{N}_{Rl} \rangle\rangle$ [51]. We use iNRG to calculate the conductance through the device from Eq. 12 at a given temperature T, as a function of B_L and B_R.

Although NRG employs a discretized representation of the conduction electron part of the model $H_{\rm elec}$ (the Wilson chains), the renormalization group structure of the model is exploited in NRG to nevertheless obtain highly accurate approximations to the exact continuum result for equilibrium physical quantities [35, 47, 50].

Device

The device was fabricated on a GaAs/AlGaAs heterostructure with a 2DEG approximately 95nm deep, density of 2.6×10^{11} cm^{-2} and mobility 2.0×10^6 cm^{2}V^{-1}s^{-1}. An SEM micrograph of an equivalent device is shown in Extended Data Fig. 2. High transparency of the small ohmic contacts is crucial, so we take special steps to ensure cleanliness of the interface with the GaAs heterostructure. Before any fabrication is done on the heterostructure, we dip in HCl 3.7% to remove any oxide layer that has built up. After writing the ohmic layer pattern using e-beam lithography and developing the PMMA resist, we use a light oxygen plasma etch to remove residual PMMA scum. Next, before evaporating the ohmic stack, we use the following chemical treatment procedure: dip in TMAH 2.5% for 20 seconds, 5 seconds in water, 5 seconds in HCl 37%, 5 seconds in water (separate from the first cup of water). Afterwards, we quickly move the chip into a KJL Lab 18 e-beam evaporator (with a load-lock), and pump down to $\sim 10^{-6}$ torr vacuum. Reducing the time in air is important to prevent substantial oxide layer growth. Finally, we run a low-power in-situ Argon etch for 20 seconds. Only after this do we evaporate the ohmic stack (107.2 nm Au, 52.8 nm Ge, and 40 nm Ni, in order of deposition).

Experimental Setup

The device was cooled down with a +300 mV bias on all the gates to reduce charge instability by limiting the range of voltages we need to apply [52]. To reduce thermoelectric noise causing unwanted voltage biasing across the device, each lead has a central ohmic contact (between the source and measurement contacts) and all those central ohmics are shorted to each other on chip. The shorted ohmics are connected to a single line and grounded at room temperature. Measurements are made at low frequencies ($<$ 100 Hz) using an SR830 lock-in amplifier. The 14 mV output of the SR830 is converted to a current bias using a 100MΩ resistor, and the current is then converted to a voltage on chip by the quantum Hall resistance ($h/2e^2$). A measurement of either the series transmitted voltage or the reflected voltage is amplified by an NF SA-240F5 room-temperature voltage amplifier. The series conductance of interest can then be simply extracted from this voltage as explained below. For most reported measurements, we source at *S2* and measure at *M2* (see Fig. 1a). The series conductance is then related to the reflected voltage, V_2 by Eq. 13.

$$G = \frac{e^2}{3h} \frac{V_2 - V_2^{\tau_{R,L,C}=0}}{V_2^{\tau_{R,L,C}=1} - V_2^{\tau_{R,L,C}=0}} \tag{13}$$

Measurements in this way eliminate the need for precise knowledge of many settings in a given setup – excitation amplitude, amplifier gain, line resistances, etc. For arbitrary sourcing and measurement configurations, the relations between measured voltages and the desired conductances can be calculated straightforwardly through Landauer–Büttiker formalism.

Electron Temperature

The electron temperature is determined from dynamical Coulomb blockade measurements outlined in Iftikhar [53]. The zero bias suppression of the conductance across a QPC when series coupled to another QPC of low resistance can be fit to a known theoretical form which directly depends on the electron temperature [54]. In our device we measure through two QPCs across a single island ($\tau_C = 0$), with one QPC partially transmitting and the other set to fully transmit a single edge mode.

Calibrating QPC Transmissions

A standard procedure to measure the transmission of each QPC is to measure the series conductance while varying the applied gate voltage of the QPC, with each other QPC set

to fully transmit n edge states, acting as an h/ne^2 resistor. For our experiments of central interest, we must then adjust each QPC to a desired transmission. We cannot naively use the gate voltages that produced that transmission with all other QPCs open, because changing the voltage applied to any gate capacitively affects all other QPCs. However, we can calibrate this capacitive effect by measuring how much each QPC's transmission curve shifts as we vary each other QPC's gate voltage by a known amount. This is done for each pair of QPCs we use in the experiment, and with this information we can systematically determine the appropriate gate voltages to set. However, even this procedure fails in our device. When transmission is measured in series through a QPC and an additional resistance on order h/e^2, dynamical Coulomb blockade (DCB) suppresses the conductance relative to that expected from ohmic addition of the 'intrinsic' transmissions [54]–[64]. The 'intrinsic' transmissions can be recaptured by applying a source-drain bias large compared to a relevant charging energy (Extended Data Fig. 3a).

Alternatively, a measurement pathway which does not go through the metal island (for example, measuring τ_R through the plunger gate P_R) effectively shorts the circuit to ground, so the 'intrinsic' transmission is recovered even at zero source drain bias [56, 65]. The measured QPC transmission at low bias avoiding the island should then be the same as the measurement at high bias through the island. Empirically, this is not the case in our device. Instead, repeating the measurement through P_R at *high bias* shows exact agreement with the high bias measurement through the island. Bias-dependent measurements through P_R show a zero-bias suppression and a high bias plateau of conductance consistent with DCB suppression, contrary to expectation that DCB should be negligible in this configuration (Extended Data Fig. 3c).

We suspect that this residual DCB effect is due to impedances in our measurement setup, external to the device. We connect our measurement lines which ground the device through highly resistive coaxial lines and discrete filters located right above the connection to the sample through large ohmic contacts. This is in contrast to earlier work ([19, 20]) on this type of system in which a cold ground is used, effectively creating a very low impedance path to ground.

The important question is which measurement transmission is relevant for the Kondo interactions. While previous work ([19, 20]) found the difference between the 'intrinsic' transmission and the zero bias transmission through an open plunger gate to be small, and thus both equally valid, we find that the measurement through P_R at zero bias empirically works best in our device. Without any residual DCB, we believe this should be the exact same as the 'intrinsic' transmission. However, the residual DCB appears to not only suppress the measured QPC transmissions, but all measured conductances of our system in any configuration, at zero bias. In particular, when measuring through either one or both islands, the conductance when using the 'intrinsic' transmission at charge degeneracy points, where Kondo interactions are most important, is consistently lower than both expectations and previous results seen in [19]. With the single island, we see a suppression consistent with DCB: the series conductance we measure at a Coulomb blockade peak is lower than that measured in [19] for the same 'intrinsic' transmissions and temperature, with the smallest differences in conductances being near the maximum (0.5 e^2/h) or minimum (0 e^2/h) possible conductances. Furthermore, the differences reduce at higher temperatures. These two features are similar to that seen in DCB measurements.

If instead we use not the 'intrinsic' transmission, but the zero bias transmissions through P_R, we see remarkably consistent agreement with previous measurements of the two-channel Kondo model for different transmissions and temperatures. Our interpretation is that while both Kondo and DCB renormalize conductance, we can work in a 'DCB-renormalized space' by explicitly setting the DCB-renormalized transmissions. These DCB-renormalized transmissions then act as the transmissions that are in turn important for the Kondo interactions. Importantly, we must use the transmissions measured in an environment in which the QPC sees the same electromagnetic impedance as in the measurements of interest. This means using the zero bias transmissions measured through P_R, where DCB is caused by only the external impedances, and not the zero bias transmissions measured through the island, where there is additional suppression due to the resistance of the second QPC in series.

On the left island, the QPC we use does not have an adjacent pathway through P_L, but due to an equivalence of the island-lead QPCs, a consistent mapping can be made from the 'intrinsic' transmission to the DCB-renormalized one that would be measured through the plunger gate. However, we are unable to make this mapping for the inter-island QPC as we observe differences in the DCB-renormalization when measured through the islands (Extended Data Fig. 3b). Likewise, we are unable to measure the extraneous DCB-renormalization of the inter-island QPC due to the device geometry. In our results in the main text, we therefore report 'intrinsic' values for τ_C and the DCB-renormalized values (measured through P_R) for τ. This may be why the maximum conductance does not appear at $\tau = \tau_C$, and in any case it means that the τ_C relevant for Kondo physics grows with increasing temperature.

The conclusions of the main text are not sensitive to the choices described above regarding which values ('intrinsic' or DCB-renormalized) we report for each QPC transmission. None of our results rely on precise quantitative knowledge of the transmission settings, since T^* depends only on detuning of one transmission relative to another. This would not be the case in any future work exploring universal scaling as a function of T/T_K, since T_K depends directly on the quantitative transmissions.

Fitting universal curves

To calculate $|\cos 2\pi U/\delta - \Delta_{TP}|^{3/2}$ and thus T^* first requires extracting δ, Δ_{TP}. As mentioned in the main text, these relate to the triple point periodicity and splitting respectively. The data of Fig. 3 are extracted from charge stability diagrams over larger gate voltage ranges like in Fig. 1c. The line cuts of Fig. 3a specifically come from averages over multiple pairs of triple points, whereas the rest of Fig. 3 uses singular line cuts. Using either line cuts from the the full stability diagram or from other stability diagrams taken with the exact same τ, τ_C values, we can extract δ and Δ_{TP}. There is uncertainty in the triple point splitting, as identifying the triple points is non-trivial, which we will discuss further below. Finally, we must also determine the unknown scaling prefactor b of Eq. 2. We do this by least-squares fitting $b|\cos 2\pi U/\delta - \Delta_{TP}|^{3/2}$ of the experimental data to T^* of the universal curve, with b as a free parameter. Each τ_C line cut is independently fit, and we average the resulting b values and apply the same rescaling to each curve. We find $b = 1$ mK works best. A similar procedure is done in Fig. 3b, except we fit only the 20 mK data to the fully universal curve, obtaining $b = 3.7$ mK. The elevated temperature data are then rescaled with that same obtained b. For every curve, we also fit a constant shift $a|\Delta\tau_C|^{3/2}$ to take into account that there is a finite T^* even at $\Delta U = 0$ due to a detuning from the critical couplings. These fits exclude the first few data points at the lowest T^*, where we do not expect agreement with the universal curve due to a finite T/T_K (with T_K the critical Kondo temperature as before).

In Extended Data Fig. 4a, we show the τ_C values used in the scaling collapse data of Fig. 3a in the main text. To resolve the TP peaks we need a sufficiently large τ_C, of which the value needed grows with τ. To reach a conductance close to $e^2/3h$ and have split triple points, τ_C must be made extremely close to 1. While one might guess that the resulting measured line cuts would be essentially identical, we see that in the full shape (Extended Data Fig. 4b) there are large changes to the line cuts even for tiny changes in $\tau_C \sim 1$. Contrast this with Fig. 2a of the main text where τ_C is far from 1, large changes in τ_C are needed for comparable changes in the line cuts.

In Fig. 3b, to roughly match the conductance at $\Delta U = 0$ across different temperature, we adjust the transmissions at each temperature. If the transmissions were instead held constant, the conductance would decrease with increasing temperature due to a larger T/T_K. By increasing τ, τ_C with temperature, T/T_K is maintained roughly constant. In our measurement, $\tau = \{0.78, 0.78, 0.81, 0.82\}$ at $T = \{20, 26, 46, 75\}$ mK while $\tau_C = 0.9$ for all T. As described in the Calibrating QPC Transmissions section of Methods, we know that this corresponds to a slightly increasing τ_C with temperature, although the exact variation is unknown. That τ_C varies between temperatures does not affect the conclusion, since the scaling as a function of ΔU is unaffected.

Finally, as previously mentioned, in some cases the TPs are not easily identifiable, depending on τ and τ_C. Though in Fig. 3 we try to choose line cuts in which the TPs are relatively well separated, it is not always possible depending on the couplings and temperature. By using NRG calculations at extremely low temperatures to determine the TP locations and comparing them to the location of the conductance peaks at higher temperatures, we can estimate the difference between conductance peak and TP position. We find from our NRG calculations that choosing a point ~ 1 μeV away from the peak conductance for the two lowest temperatures of Fig. 3b, ~ 2 μeV away for the 46 mK data, and ~ 10 μeV away for the 75 mK data is a good approximation. The large offset of the 75 mK data is simply due to there only being a single conductance peak centered between the two TPs at this temperature. We find that this set of offsets is equivalent to what we would obtain by assuming the triple point splitting, and thus Δ_{TP}, is constant for all the temperatures, which is valid since τ, τ_C do not vary much between them. For all of the data used in Fig. 3a, where the TPs are well separated, we find that using the conductance peak location as the TP location is a good approximation. Due to a combination of an imperfect identification of the TP location and finite spacing of measurements in gate voltage, there will still be some error in choosing the true TP location. We estimate this uncertainty in ΔU to be ~ 0.25 μeV for all data taken at the two lowest temperatures, and ~ 1 μeV for the two higher temperatures. Though any uncertainty in ΔU creates a non-linear error when scaling ΔU to T^*, we find that changes within the uncertainty of where we set $\Delta U = 0$ do not significantly change our results. We see this by offsetting ΔU and redoing the same scaling collapse analysis.

For the orthogonal line cuts, we instead fit the scaling prefactor b in Eq. 2 of the 20 mK data to the universal curve, finding $b = .0086$ mK/μeV$^{3/2}$. As in the parallel line cuts, all higher temperatures use the same prefactor.

Metal-2DEG Interface

To apply our model to our experimental system, the edge modes in the 2DEG transmitted through a quantum point contact must then be perfectly transmitted into the metal component. For this to occur, first, the edge mode must not bypass the metal. To enforce this, following Iftikhar ([19]), trenches are etched in the 2DEG below the island so the metal is the only conducting path bridging otherwise separate regions of 2DEG on different mesas. Second, reflection of the edge mode from the metal must be minimal. We verify near-perfect transmission by relating measured voltages to the transmission into the metal $\tau_\Omega^{R,L}$. In principle it is possible to extract the separate transmission probabilities for each metal-2DEG interface, but here we report an average. Unlike in the work of Iftikhar ([19]), we find we must take into account the non-negligible resistance to ground in our setup – through cryostat lines and filters intended to maintain low electron temperature – which generates a finite transmitted voltage

$V_T^{\tau_i=0}$, even with all QPCs closed.

$$\frac{V_{2(1)}^{\tau_{R(L),4(3)}=1,\tau_C=0} - V_T^{\tau_i=0}}{V_{2(1)}^{\tau_i=0} - V_T^{\tau_i=0}} = 1 - \tau_\Omega^{R(L)}/4 \qquad (14)$$

Here $\tau_{3,4}$ are the unused QPCs in our experiment, representing the transmissions of the bottom QPCs of the left and right islands respectively. In our device, we measure

$$\tau_\Omega^R = 1.0004 \pm 0.0098 \qquad \tau_\Omega^L = 0.9947 \pm 0.0417$$

There is a much larger uncertainty on the left island, due to a noisier measurement contact $M1$.

Measurement Uncertainty

A few factors contribute to uncertainty in the reported conductance. Due to slow drift in the electric potential, we cannot reliably sit at the same position in the charge stability diagram. This reduces the ability to average over time at a particular configuration of P_L, P_R. Based on the standard deviation in conductance in a configuration where each QPC was fully open, this error is $\sim 0.001\ e^2/h$.

There is a second uncertainty in that the conductance for a given pair of triple points varies between periods in P_L, P_R. We observe that repeated measurements center around a particular value, with a few clear outliers of much lower conductance. To reduce this effect, we take the median conductance over a few periods. Reducing the error is limited by needing to remeasure the full charge stability diagram multiple times. For example, the data in Fig. 2a are extracted from 141 charge stability diagrams, of which about only 40 had no clear charge switching events along the line between triple points. The errors of Fig. 2a for a particular τ_C and U (median absolute deviation $\sim 0.006\ e^2/h$) are such that the exact τ_C line cut in which the conductance peaks at $U = 0$ is unknown, but the overall non-monotonic behavior is unchanged.

Charging events may also infrequently shift the set transmission of one of the QPCs. Thus, for each 2D sweep we recalibrate each QPC to ensure we are at the transmission stated. The QPC calibration procedure relies on the accurate determination of the cross-talk between QPCs. While in principle this can be done very accurately, we cannot explicitly verify the transmissions in the experimental configurations used in our main results. However, we can verify that the procedure works by looking at the symmetry of the charge stability diagrams, which depends on the two island-lead QPCs having equal transmissions. From this we estimate that the transmissions are off from their intended values by at most 0.03.

Finally, our conversion from voltage to conductance could introduce errors due to uncertainties in our measurement electronics. However, we can calibrate out these uncertainties by normalizing our measured voltages by the reflected voltage with all QPCs closed (Methods). Any error is likely due to any imperfections in the metal-2DEG interface, as our conversion from voltage to conductance assumes $\tau_\Omega = 1$. When this assumption is broken, the reported series conductance values would both be off from the true series conductance, and the true series conductance would not be the right comparison to our NRG results, as the DCK model also assumes a perfect metal-2DEG transparency. Using our measurements of τ_Ω above, we estimate that our reported series conductance values have an error of $\sim 1\%$, coming from $\left|1 - \tau_\Omega^L\right| \sim .01$.

Data Availability

All data used in this work are available in the Stanford Digital Repository at https://doi.org/10.25740/mx151nn9365.

References

[47] Wilson, K. G. The renormalization group: Critical phenomena and the Kondo problem. *Rev. Mod. Phys.* **47**, 773–840 (1975).

[48] Stadler, K. M., Mitchell, A. K., von Delft, J. & Weichselbaum, A. Interleaved numerical renormalization group as an efficient multiband impurity solver. *Phys. Rev. B* **93**, 235101 (2016).

[49] Galpin, M. R. *et al.* Conductance fingerprint of majorana fermions in the topological kondo effect. *Phys. Rev. B* **89**, 045143 (2014).

[50] Weichselbaum, A. & von Delft, J. Sum-Rule Conserving Spectral Functions from the Numerical Renormalization Group. *Phys. Rev. Lett.* **99**, 076402 (2007).

[51] Minarelli, E. L., Rigo, J. B. & Mitchell, A. K. Linear response quantum transport through interacting multi-orbital nanostructures. *arXiv preprint arXiv:2209.01208* (2022).

[52] Pioro-Ladrière, M. *et al.* Origin of switching noise in $GaAs/Al_xGa_{1-x}As$ lateral gated devices. *Phys. Rev. B* **72**, 115331 (2005).

[53] Iftikhar, Z. *et al.* Primary thermometry triad at 6 mK in mesoscopic circuits. *Nat Commun* **7**, 12908 (2016).

[54] Joyez, P. & Esteve, D. Single-electron tunneling at high temperature. *Phys. Rev. B* **56**, 1848–1853 (1997).

[55] Souquet, J.-R., Safi, I. & Simon, P. Dynamical Coulomb blockade in an interacting one-dimensional system coupled to an arbitrary environment. *Phys. Rev. B* **88**, 205419 (2013).

[56] Altimiras, C., Gennser, U., Cavanna, A., Mailly, D. & Pierre, F. Experimental Test of the Dynamical Coulomb Blockade Theory for Short Coherent Conductors. *Phys. Rev. Lett.* **99**, 256805 (2007).

[57] Senkpiel, J. *et al.* Dynamical Coulomb Blockade as a Local Probe for Quantum Transport. *Phys. Rev. Lett.* **124**, 156803 (2020).

[58] Jezouin, S. *et al.* Tomonaga-Luttinger physics in electronic quantum circuits. *Nat Commun* **4**, 1802 (2013).

[59] Flensberg, K., Girvin, S. M., Jonson, M., Penn, D. R. & Stiles, M. D. Quantum mechanics of the electromagnetic environment in the single-junction coulomb blockade. *Phys. Scr.* **1992**, 189 (1992).

[60] Yeyati, A. L., Martin-Rodero, A., Esteve, D. & Urbina, C. Direct Link between Coulomb Blockade and Shot Noise in a Quantum-Coherent Structure. *Phys. Rev. Lett.* **87**, 046802 (2001).

[61] Pekola, J. P., Holmqvist, T. & Meschke, M. Primary Tunnel Junction Thermometry. *Phys. Rev. Lett.* **101**, 206801 (2008).

[62] Golubev, D. S. & Zaikin, A. D. Electron transport through interacting quantum dots in the metallic regime. *Phys. Rev. B* **69**, 075318 (2004).

[63] Devoret, M. H. *et al.* Effect of the electromagnetic environment on the Coulomb blockade in ultrasmall tunnel junctions. *Phys. Rev. Lett.* **64**, 1824–1827 (1990).

[64] Parmentier, F. D. *et al.* Strong back-action of a linear circuit on a single electronic quantum channel. *Nature Phys* **7**, 935–938 (2011).

[65] Slobodeniuk, A. O., Levkivskyi, I. P. & Sukhorukov, E. V. Equilibration of quantum Hall edge states by an Ohmic contact. *Phys. Rev. B* **88**, 165307 (2013).

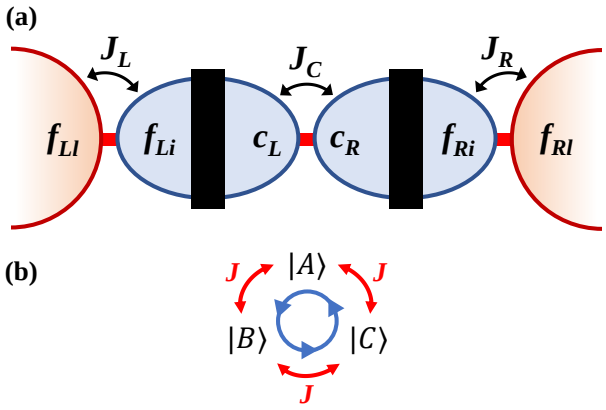

Extended Data Fig. 1: Schematic illustrations of the models discussed. a, The DCK model consists of six effectively independent spinless conduction electron reservoirs (blue for island, red for lead), described by fermionic operators $f_{\alpha\gamma}$ and c_α for $\alpha = L, R$ and $\gamma = l, i$. Tunneling occurs at each of the three QPCs controlled by $J_{L,C,R}$. The island charging energy E_C^α correlates electrons $f_{\alpha i}$ and c_α on the same island either side of the metal component (black bar). **b**, At a TP, Eq. 9 describes the system at low temperatures. The three retained charge states of the two-island structure (denoted $|A\rangle, |B\rangle, |C\rangle$) are interconverted by QPC tunneling. The frustrated QCP arises when $J_L = J_R = J_C \equiv J$. The conductive pathway $|A\rangle \to |B\rangle \to |C\rangle$ corresponds to transport from left lead to right lead, and is illustrated with the blue arrows (the flow is reversed $|C\rangle \to |B\rangle \to |A\rangle$ by changing the sign of the applied bias voltage).

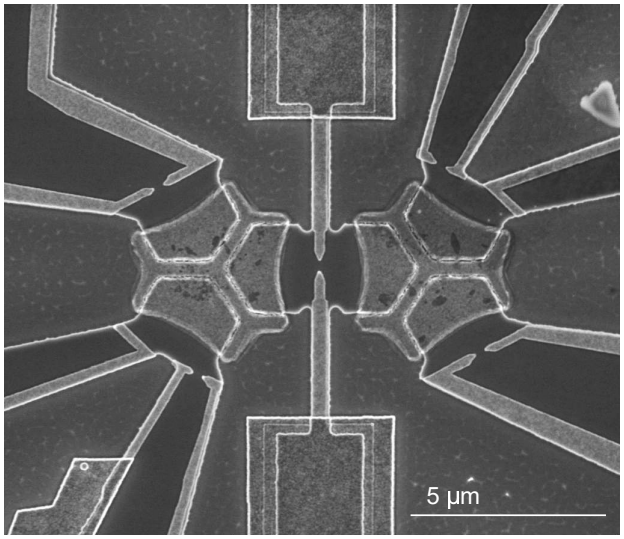

Extended Data Fig. 2: SEM micrograph of nominally identical device.

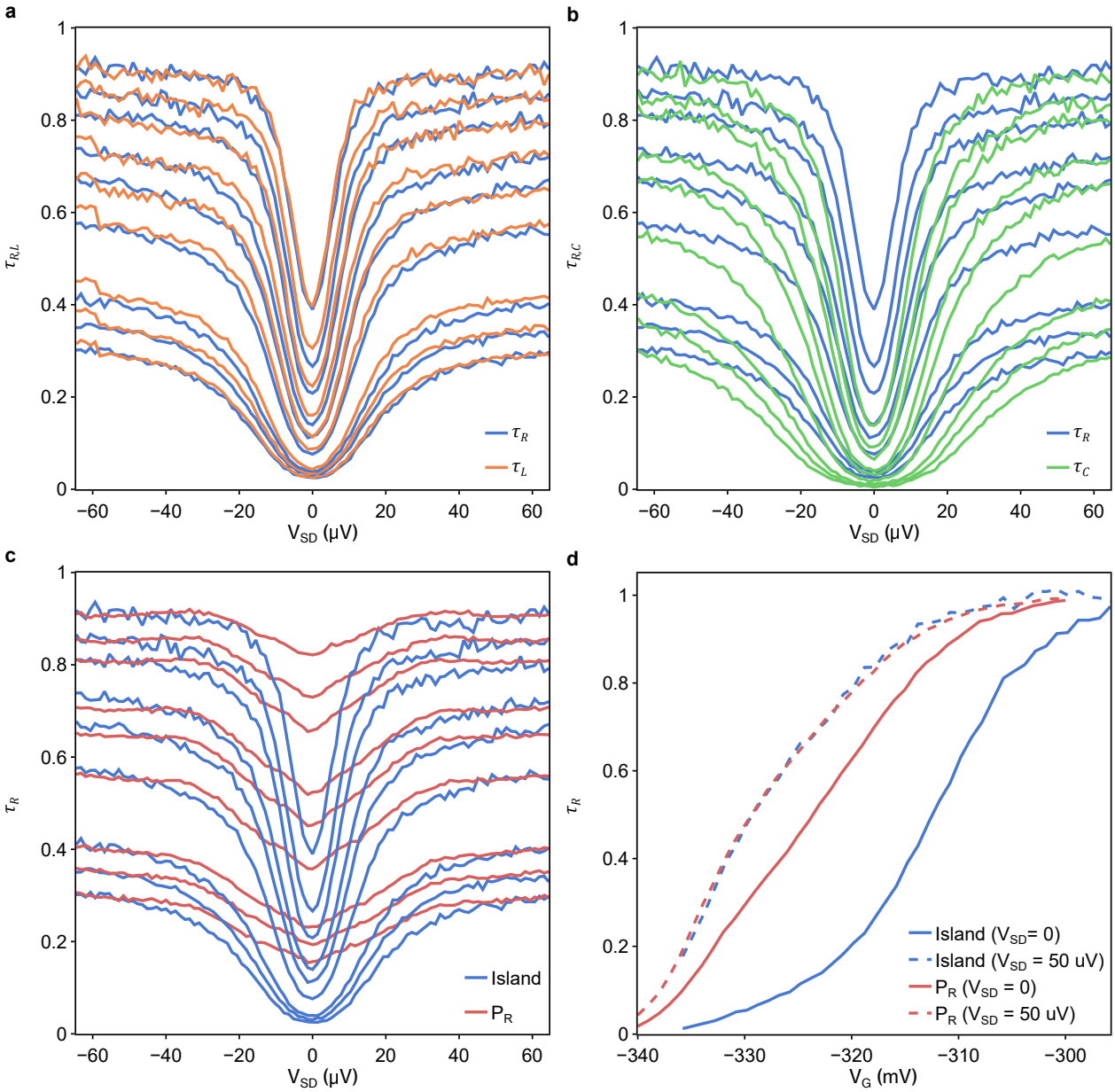

Extended Data Fig. 3: Dynamical Coulomb blockade of QPC transmissions. a. Measured QPC transmissions τ_R, τ_L as a function of a source-drain bias V_{SD} for different QPC gate voltages. The measured transmission is extracted by measuring the series conductance when in series with the inter-island QPC and opposite island-lead QPC set to fully transmit a single channel ($\tau_{C,L/R} = 1$). The measured transmissions clearly dip at zero bias, consistent with dynamical Coulomb blockade (DCB) behavior. The high bias behavior ($V_{SD} \approx 50$ uV) recovers the 'intrinsic' transmission of the QPC, unrenormalized by DCB. **b.** DCB measurements comparing the right island-lead QPC to the inter-island QPC. It is clear there is a substantial difference in the DCB-renormalization at zero bias between the two, likely due to the device geometry. **c.** Comparison of measuring τ_R through both islands (blue lines, as in **a, b**) and through the adjacent plunger gate P_R (red lines). While typically we would expect no significant bias dependence when measuring through P_R, we in fact see DCB-like behavior. **d.** Comparing the two measurement pathways of **c** at fixed source-drain bias as a function of the QPC gate voltage. The 'through the island' (blue) measurements have been shifted by 9 mV to account for the large capacitive cross-talk effect when switching between the two different measurement pathways. That the high bias traces match well is indicative that there is indeed DCB-renormalization of the transmission when measuring through P_R. Empirically, using the zero bias, 'through the plunger gate' measurement of the transmission (solid red line), best captures the relevant transmissions in the Kondo interactions of our system.

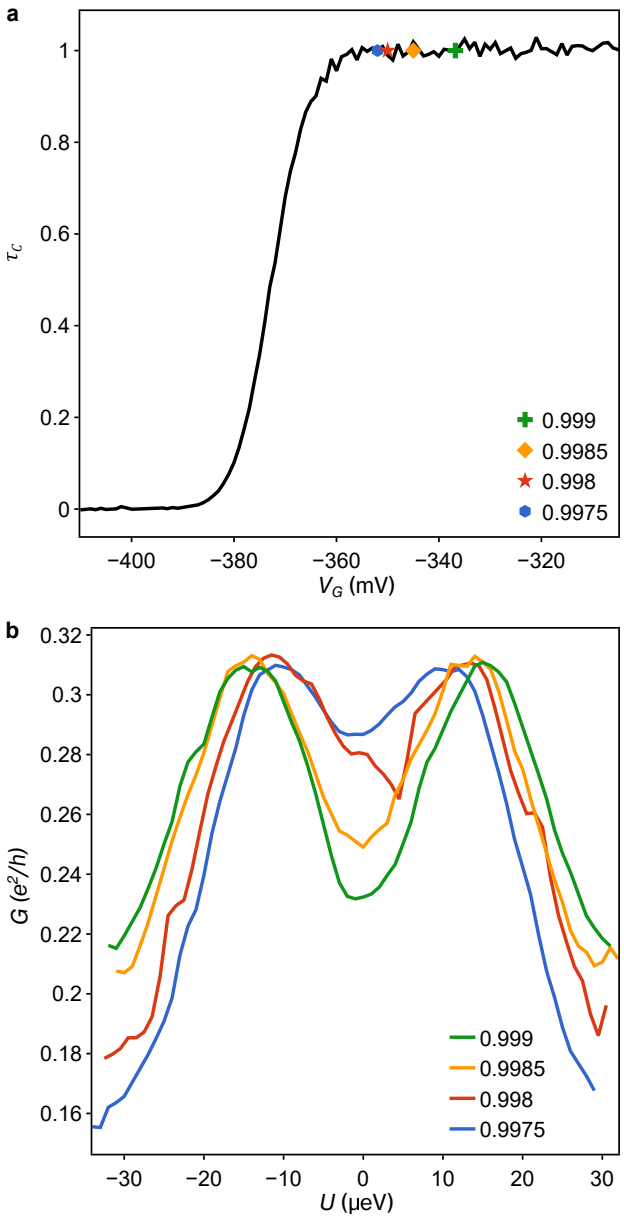

Extended Data Fig. 4: Semi-universal τ_C values. a, Measured inter-island transmission as a function of an applied gate voltage. The markers correspond to the inter-island transmissions used in Fig. 3a of the main text. **b,** Original line cuts in which the truncated data used in Fig. 3a are extracted from.

SUPPLEMENTARY INFORMATION

Alternative T^* scaling

A natural question is whether our experimental system could be realized by an alternative model. Demonstrating that an experimental system is a realization of a particular theoretical model is always complicated, since the space of possible alternative models and refinements is in principle infinite. That said, the universality classes that emerge from renormalization group analysis offer one way of distinguishing different classes of models and of identifying which could satisfactorily describe experimental data. We believe the scaling collapse to a universal curve using a non-trivial power law is remarkable and is the unique signature of the critical point studied. However, the experimental data alone are not sufficient to definitively distinguish the power law from another close one. It is the overall consistency between experiment and theory in all features which validates the model. Not only is our model the natural one for the system we have constructed, but we are aware of no alternative model whose predictions are consistent with all of our experimental results, as our NRG results are.

However, we can still do the same scaling collapse analysis assuming an alternative power law and observing the results. Explicitly, we assume $T^* = T_0^* + b|\cos 2\pi U/\delta - \Delta_{TP}|^\gamma$, where $T_0^* = a|\Delta\tau_C|^\gamma$, and plot the results in Supplementary Fig. 1b for $\gamma = 1$ (other power laws such as $1/2$ or 2 clearly do not work). As we outline in Methods, we generally need to fit an unknown shift T_0^* since we do not have direct knowledge of the deviation away from the critical couplings. When $\gamma = 1$ instead of $3/2$, there is no physically-motivated universal curve, so instead of finding T_0^* by best fit to a universal curve, we apply a shift $T_0^* = a|\Delta\tau_C|$ such that the data best collapses onto itself.

We see that the experimental data are plausibly consistent with the power law of 1, but there are a few subtle deviations. Particularly, the end of the 26 and 46 mK temperature line cuts deviate from the 20 mK one. While there is a somewhat arbitrary horizontal offset, we cannot simultaneously well align the low T^*/T and high T^*/T behavior.

Finally, we also plot the orthogonal line cuts with a $T^* = T_0^* + |\Delta U|^1$ scaling in Supplementary Fig. 1d. This data clearly does not collapse well with a power law of 1, demonstrating that it is indeed a 3/2 power law which governs the behavior of our system. We attribute the differences in how well the power law of 1 works in the parallel vs orthogonal line cuts to the diminished influence of higher charge states in the orthogonal direction, as mentioned in the main text.

While the above analysis suggests $\gamma = 3/2$, we acknowledge that definitively determining the relevant power law from experiment alone would require a larger range of temperatures. Since there is a clear limit on how high in temperature our model should hold, obtaining a larger temperature range would require reaching even lower temperatures or larger charging energies. It is the consistency of experimental data with the 3/2 power law combined with a broader set of agreement with NRG results that gives confidence that we are indeed observing the DCK model.

Competition between Kondo interactions

The critical point in our system arises from a frustration of different competing Kondo effects. To understand the nature of the critical point, it is instructive to consider the limits where one of the Kondo effects dominate. We again focus on the TP.

First, take the DCK model with inter-island coupling $J_C = 0$ and $J_R = 0$ but $J_L > 0$. In this case, the charge pseudospin of the left island is exactly Kondo-screened by coupling to the left lead via the term $J_L(\hat{\mathcal{S}}_L^+ \hat{s}_L^- + \hat{\mathcal{S}}_L^- \hat{s}_L^+)$ (that is, the charge configurations $|N, M\rangle$ and $|N+1, M\rangle$ are lowered in energy relative to $|N, M+1\rangle$ and participate in a single-channel Kondo effect). This process happens on a single-channel

Kondo scale $T_{K,L}^{(1)} \sim E_C \exp[-1/2\nu J_L]$. Likewise for $J_C = 0$ and $J_L = 0$ but $J_R > 0$, the right island charge pseudospin undergoes a single-channel Kondo effect with the right lead on the scale of $T_{K,R}^{(1)} \sim E_C \exp[-1/2\nu J_R]$.

Next, consider the limit $J_L = J_R = 0$ but $J_C > 0$. Here the leads are cut off from the islands, but the inter-island coupling remains active. The TP charge configurations $|N, M+1\rangle$ and $|N+1, M\rangle$ are interchanged by tunneling at the central QPC, and are therefore lowered in energy relative to $|N, M\rangle$. Writing $\hat{\mathcal{S}}_C^+ = |N+1, M\rangle\langle N, M+1|$ and $\hat{\mathcal{S}}_C^- = |N, M+1\rangle\langle N+1, M|$ in this reduced subspace, and relabelling $c_L \to c_\downarrow$ and $c_R \to c_\uparrow$ such that $\hat{s}_C^+ = c_\uparrow^\dagger c_\downarrow$ and $\hat{s}_C^- = c_\downarrow^\dagger c_\uparrow$, the inter-island coupling takes the form of a single-channel Kondo interaction $J_C(\hat{\mathcal{S}}_C^+ \hat{s}_C^- + \hat{\mathcal{S}}_C^- \hat{s}_C^+)$. Thus we again expect Kondo screening of the two-island charge degrees of freedom by a single-channel Kondo effect on the scale of $T_{K,C}^{(1)} \sim E_C \exp[-1/2\nu J_C]$.

In each of these cases, the systems flows to a Fermi liquid ground state with a completely quenched residual ($T = 0$) entropy and fully screened island charge degrees of freedom.

When J_L, J_R, and J_C are all finite, the three Kondo effects compete. However, they cannot arise simultaneously because each binds two of the three charge states at the TP into a singlet with conduction electrons. This leads to frustration when $T_{K,L}^{(1)} = T_{K,R}^{(1)} = T_{K,C}^{(1)}$ which in fact implies the condition $J_L = J_R = J_C \equiv J$ (contrast with the conventional 2IK model, Eq. 15, where the critical point occurs when $J_C \sim T_{K,L/R}^{(1)} \ll J_{L/R}$). This leads to a critical point with a non-Fermi liquid ground state and only partially screened island degrees of freedom, yielding the unusual $\ln(\sqrt{3})$ residual entropy reported in the main text. The system flows to this critical point on the scale of the critical Kondo temperature, which has a slightly modified exponent relative to its single-channel counterparts, $T_K \sim E_C \exp[-1/\nu J]$, again as reported in the main text.

Finally, consider the case where the critical point is perturbed by a symmetry-breaking term in the Hamiltonian. This can either be a detuning of the coupling $J_C \neq J$ (with $J_L = J_R \equiv J$ such that $\delta J = J_C - J$), or a detuning in gate voltage away from the TP, denoted ΔU in the main text. Such terms generate a new scale T^* characterizing the flow to the single stable fixed point of the DCK model, describing a Fermi liquid ground state. If these perturbations are large (meaning in practice $|\delta J|, |\Delta U| > T_K$) then signatures of the QCP are not observed. For a coupling detuning $|\delta J| > T_K$, the system flows to a Kondo-screened Fermi liquid state on the scale of $T^* \sim T_K^{(1)}$ ($> T_K$); while for gate detuning $|\delta U| > T_K$ the system flows to a frozen-charge Fermi liquid ground state on the scale of $T^* \sim |\Delta U|$. More interesting is the case of small perturbations $|\delta J|, |\Delta U| < T_K$, since then the system first flows close to the QCP (on the scale of T_K) and then away again, and toward the Fermi liquid ground state on the scale of T^* ($< T_K$), as given by Eq. 2 of the main text. For $T^* \ll T_K$ we have an intermediate window in temperature $T^* < T < T_K$ where the system exhibits critical behavior. NRG results illustrating this are shown in Supplementary Fig. 2. This is the regime we seek to explore experimentally in the present work.

The above results and conclusions were gleaned from our NRG results on the DCK model. Now we turn back to the experiment.

The competition of Kondo screening described above is reflected experimentally in the behavior of conductance as the QPC transmissions τ and τ_C are varied. In Supplementary Fig. 3, we show experimentally how the conductance is most enhanced when the island-lead and inter-island Kondo interactions are of comparable strength. As τ is increased, the maximum conductance (for any U) occurs at increasing τ_C. τ_C^* is determined as the particular τ_C value for which the maximum occurs. While naively we might expect the relation between τ_C^* and τ to be linear (since the Kondo interactions are equal for $J = J_C$), it is not necessarily true that the mapping of $\tau \to J$ and $\tau_C \to J_C$ are the same. Furthermore, the reported values of τ and τ_C differ due to differences in how they are measured (see Methods).

Fitting and model parameters

Analysis of the experimental Coulomb diamond measurements (Supplementary Fig. 4) yields $E_C^L \simeq E_C^R \simeq 25$ μeV and the lever arm $\alpha = 50$ μeV/mV (which is assumed to be independent of other device parameters and temperature). We estimate $I \simeq 10$ μeV from the triple point splittings (taking into account the renormalization due to τ_C). We use these values in our NRG calculations, together with the conduction electron bandwidth $D = 250$ μeV (we have verified explicitly that our computational results are insensitive to further increasing the ratio D/E_C, the precise choice of which is somewhat arbitrary). To obtain converged results at larger QPC transmissions, we retain 16 charging states of each island ($\bar{N} = \bar{M} = 7$). Comparisons between experiment and theory are carried out at the experimental base electron temperature of 20 mK.

Although a precise mapping between the QPC transmissions $\tau_{L,R,C}$ and $J_{L,R,C}$ exists in the idealized ballistic limit of noninteracting electrons at a constriction, this approximation was found to be too crude to reproduce even qualitative features of the experiment for this more complex system. Instead, we treated the model couplings $J_{L,R,C}$ as free parameters. For a given set of experimental transmissions $\tau_{L,R,C}$ we compared the conductance line cut along the line $U_L = U_R$ to NRG calculations to fix the optimal $J_{L,R,C}$ reported in the main text. Empirically, we do find a rather simple relation between τ_C and J_C: roughly linear up to $\tau_C = 0.8$ ($J_C = 0.4$) where the relation becomes slightly non-linear.

Cross-capacitive gate effects

B_L and B_R in the model can be connected to the experimental parameters U_L and U_R via $\vec{B} = \bar{\boldsymbol{\alpha}}\vec{U}$. Off-diagonal elements of the dimensionless 2x2 matrix $\bar{\boldsymbol{\alpha}}$ correspond to cross-capacitive gate effects. In fitting to the

experimental data, we used $\bar{\boldsymbol{\alpha}}_{LL} = \bar{\boldsymbol{\alpha}}_{RR} = 1$ and $\bar{\boldsymbol{\alpha}}_{LR} = \bar{\boldsymbol{\alpha}}_{RL} = 0.3$. The unskewed conductance color plot in the space of the NRG parameters (B_L, B_R) corresponding to Fig. 1d is shown for reference in Supplementary Fig. 5.

Relation to two-impurity Kondo model and to "conventional" double quantum dots

In the limit of large charging energies $E_C^{L,R}$, the two-site charge-Kondo device is described by the DCK model Eq. 1, with spin-$\frac{1}{2}$ operators for the island charge pseudospins. The DCK model is as such a variant of the celebrated two-impurity Kondo (2IK) model Eq. 15, in which two spin-$\frac{1}{2}$ quantum impurities are each coupled to their own lead and exchange-coupled together [4, 30, 66]–[70]. The 2IK model reads,

$$H_{\rm 2IK} = H_{\rm elec} + J_L \vec{\mathcal{S}}_L \cdot \vec{s}_L + J_R \vec{\mathcal{S}}_R \cdot \vec{s}_R + J_C \vec{\mathcal{S}}_L \cdot \vec{\mathcal{S}}_R \,. \quad (15)$$

The above 2IK model has some similarities and differences to the DCK model studied in this work, which we elucidate in this section.

On the level of the effective models themselves, the two key differences between Eqs. 1 and 15 are (i) the exchange coupling terms in the DCK model are anisotropic, containing only the spin-flip terms, whereas in the 2IK model they are SU(2) symmetric; and (ii) the inter-impurity coupling in the 2IK model is a simple local exchange interaction, whereas in the DCK model it is a correlated tunneling process involving electrons at the central QPC. In terms of differences in the resulting physics, the coupling anisotropy of the DCK model in (i) is unimportant, since under renormalization [47] at low temperatures, the couplings become effectively isotropic, as in the 2IK model. However, the inter-island coupling term of the DCK model in (ii) makes a dramatic difference.

Although both DCK and 2IK embody a competition between individual Kondo screening of the spins of the two sites and inter-site screening, the latter is a simple two-body *local* singlet in the 2IK model but a many-body *Kondo* singlet spanning both sites in the DCK model. An obvious sign of this difference is that the frustration of screening responsible for quantum criticality sets in at $J_C \sim T_K$ for the 2IK model [67], but for the DCK model this occurs at $J_C \sim J_L, J_R$. This can be seen in Supplementary Fig. 3, where the greatest conductance enhancement is for $\tau_C^* \sim \tau$ rather than $\tau_C^* \ll \tau$.

At the 2IK critical point, the non-Fermi liquid fixed point properties [67] of the 2IK model can be understood in terms of the two-channel Kondo model [70], in which two relevant degrees of freedom of the two-site cluster are 'overscreened' by two spinful conduction electron channels. By contrast, at the critical triple point of the DCK model we have three collective states of the two-site cluster being overscreened by three effective conduction electron channels. This leads to very different critical properties, including for example a 2IK residual entropy of $S_{\rm imp} = \ln\sqrt{2}$ but $S_{\rm imp} = \ln\sqrt{3}$ in the DCK model, and different conductance signatures (the most stark of which being the $2e^2/h$ maximum conductance with square-root temperature corrections in 2IK, but $e^2/3h$ conductance with $2/3$ power temperature corrections in DCK). To our knowledge, the DCK model supports an entirely different kind of critical point.

The quantum phase transition in the standard 2IK model [30] is often argued to capture the competition in f-electron heavy fermion systems between Kondo screening of local moments by conduction electrons, and magnetic ordering of the local moments driven by a through-lattice RKKY exchange interaction. However, heavy fermion materials contain a lattice of many local moments immersed in a *common* reservoir of mobile electrons, whereas the 2IK considers just two local moments, and two *distinct* electron reservoirs, with a purely local inter-impurity spin exchange. In the 2IK model, the artificial separation into two distinct conduction channels means that its specific critical point is not found in real heavy fermion systems. Furthermore, a similar problem arises when attempting to realize 2IK criticality in "conventional" (small, semiconductor) double quantum dot devices, described by an effective two-impurity Anderson model [34]. The very charge fluctuations on the dots required to mediate a series current spoil the independence of the channels, and thereby smooth the 2IK quantum phase transition into a crossover [33]. Indeed, even incipient signatures of 2IK criticality have never been observed experimentally in any double quantum dot or bulk system.

By contrast, the DCK model describing the two-site charge Kondo device does support a quantum phase transition, and distinctive transport signatures of it have been observed in our experimental setup. Furthermore, the *collective* many-body screening of the two sites mediated by conduction electrons in our system is more directly analogous to the low-temperature development of lattice coherence in real bulk heavy fermion materials.

Finally, we comment on the differences between our two-site charge-Kondo device and a standard double quantum dot system, which does not implement 2IK due to charge fluctuations as noted above. In our device, we see a regular hexagonal charge stability diagram (Fig. 1), with relatively high conductance along lines separating different charge configurations on the two sites (with the highest conductance being at or very near the triple point). At the triple point for $\tau_C = \tau_C^*$, there is a genuine quantum critical point. This is in contrast to the two-impurity Anderson model (2IAM), a model for a semiconductor double dot system that is more realistic than 2IK in that it allows for inter-dot tunneling. The conductance both at and near the DCK critical point is strongly dependent on temperature at low T. At the critical point, conductance is enhanced following a universal temperature dependence controlled by the Kondo scale T_K (the Kondo scale has not yet been explored experimentally); away from the critical point, as T is decreased further, conductance is suppressed following a different universal curve controlled by the Fermi liquid scale T^*, which is observed experimentally in Fig. 3. We simply require $|J_C - J_{L,R}| > 0$ to favor the inter-island ($J_C > J_{L,R}$) or island-lead ($J_C < J_{L,R}$) Kondo effect, either of which is predicted to drive the series

conductance to exactly zero in the low-temperature limit. Even for small $|J_C - J_{L,R}| > 0$ we still predict and experimentally observe a dramatic low-T conductance suppression, and a strong temperature dependence.

By contrast, in the standard double quantum dot, the exact form of the temperature dependence differs for different regimes. For strong inter-dot coupling, such that J_C is much stronger than the dot-lead Kondo temperature T_K, the conductance is suppressed for all $T \ll J_C$. Likewise there is a conductance suppression when $T_K \gg J_C$, although the physical interaction is different (RKKY-like inter-dot singlet compared to a Kondo singlet). That there is a conductance suppression on either side of $J_C = T_K$ is qualitatively similar to the DCK system, where we observe non-monotonicity in the conductance as a function of τ_C (Fig. 2a). However, the non-monotonicity in 2IAM is not necessarily expected at the triple point like in DCK, and in 2IAM when $J_C \sim T_K$ (but not equal) the conductance is only weakly temperature dependent and remains finite even as $T \to 0$, in contrast to the DCK model where there is a strong temperature-dependent suppression of conductance for even small detunings. This reflects the fact that in the DCK model there is a quantum critical point whereas in a normal semiconducting dot system there is only a crossover. Furthermore, as stated in the main text, the distinctive maximum $e^2/3h$ conductance could not be realized in 2IAM, particularly due to the presence of spin. Thus, even ignoring the quantitative differences in the temperature dependence between the two systems, non-monotonic conductance as a function of couplings, with a maximum at $e^2/3h$, constitutes a unique signature of the DCK system.

To summarize, there are clear theoretical differences in the couplings, energy scales, and temperature dependence between the DCK model and realistic models of two semiconductor dots. In this work we experimentally observe the very specific scaling behavior with temperature (Fig. 3b) that is only expected for the critical point in the DCK model.

Finally, with regards to the presence of spin in a semiconductor double dot system, there is a clear odd-even filling effect in standard spinful double quantum dots, with Kondo-boosted conductance only manifest when one or other of the dots has an odd number of electrons and carries a net spin-$\frac{1}{2}$. In contrast, in the DCK system the physical electrons are effectively spinless, and Kondo physics arises due to charge degeneracies rather than spin degeneracies, so there are no odd-even effects and every hexagon in the charge stability diagram is equivalent to every other one. In a spinless semiconducting dot system, the physics is simpler, as no Kondo effect could be present with inter-dot tunneling, precluding any strong renormalization effects.

Outlook for scaling to more complex clusters

Technical improvement of the materials platform for devices could be crucial to enable scaling to larger clusters. Switching to InAs-based quantum wells would allow boosting the charging energy [71] – and thus Kondo temperature – by shrinking the islands, without sacrificing the other demanding requisites such as well-defined quantum Hall edge states, high-transparency of miniature ohmic contacts to those edges, and quantum point contacts that smoothly tune transmission of the edge modes. This would increase our window of temperature over which conduction could be described as universal, and improve our ability to isolate the behavior near critical points even at strong coupling. As more islands are coupled together, measuring near a particular set of near-degenerate charge states, with limited influence from higher-energy states, becomes even more important and challenging.

Derivation of DCK model

Here we provide further details on the derivation of the DCK model – Eq. 1 of the main text. It is to be read in the conjunction with the Methods section of the paper and Extended Data Fig. 1. Our analysis follows the pioneering work by Matveev and coworkers in Refs. [29, 31, 32] and further developed in Refs. [72, 73].

We start with the microscopic Hamiltonian,

$$\mathcal{H}' = \mathcal{H}'_{\rm elec} + \mathcal{H}'_{\rm QPC} + \mathcal{H}'_{\rm int} + \mathcal{H}'_{\rm gate} \tag{16}$$

with $\mathcal{H}'_{\rm elec} = \sum_{\alpha,\gamma,k} \epsilon_k \psi^\dagger_{\alpha\gamma k}\psi_{\alpha\gamma k} + \sum_{\alpha,k} \epsilon_k \phi^\dagger_{\alpha k}\phi_{\alpha k}$ describing the six electronic reservoirs, with $\alpha = L, R$ for left or right, and $\gamma = l, i$ for lead or island. Tunneling at each QPC is described by,

$$\mathcal{H}'_{\rm QPC} = \sum_\alpha J_\alpha \left(\psi^\dagger_{\alpha l}\psi_{\alpha i} + \text{H.c.}\right) + J_C \left(\phi^\dagger_L \phi_R + \text{H.c.}\right) , \tag{17}$$

where we have utilized the definitions of the localized orbitals at the QPC positions, $\psi_{\alpha\gamma} = \sum_k \xi_k \psi_{\alpha\gamma k}$ and $\phi_\alpha = \sum_k \xi_k \phi_{\alpha k}$, with expansion coefficients ξ_k.

Electronic interactions on the islands are described by [31],

$$\mathcal{H}'_{\rm int} = \sum_{\alpha,\beta} \frac{\hat{Q}_\alpha \hat{Q}_\beta}{2C_{\alpha\beta}} , \tag{18}$$

with $\alpha, \beta \in L, R$. Here C_{LL} and C_{RR} are the capacitances of the L and R islands, and $C_{LR} = C_{RL}$ is the inter-island cross-capacitance. We define the charging energies $E_C^\alpha = e^2/2C_{\alpha\alpha}$ and write $I = e^2/C_{LR}$. The total charge operator for island $\alpha = L, R$ is specified by $\hat{Q}_\alpha = e\sum_k \left(\psi^\dagger_{\alpha ik}\psi_{\alpha ik} + \phi^\dagger_{\alpha k}\phi_{\alpha k}\right)$.

The effect of local potentials and external gate voltages is described by,

$$\mathcal{H}'_{\rm gate} = \sum_\alpha B'_\alpha \hat{Q}_\alpha / e , \tag{19}$$

where the total potential on island $\alpha = L, R$ is given by $B'_\alpha = B^0_\alpha + B_\alpha$. Here the reference B^0_α determines the island occupancy when no gate voltages are applied, and B_α accounts for the change due to applied gate voltages.

The experimental plunger gate voltage P_α applied to island $\alpha = L, R$ is related to the energy $U_\alpha = U^0_\alpha + A_\alpha P_\alpha$, relative to the offset reference U^0_α, via the experimentally measurable capacitive lever arm A_α. Cross-capacitive gate effects result

in a skewing of the charging diagram in gate-voltage space, but can be accounted for by writing $\vec{B}' = \bar{\boldsymbol{\alpha}}\vec{U}$, and fitting the dimensionless 2x2 matrix $\bar{\boldsymbol{\alpha}}$ to experimental results.

U(1) charge is conserved separately in each of the three conduction electron channels ψ_{Ll}/ψ_{Li}, ψ_{Rl}/ψ_{Ri} and ϕ_L/ϕ_R.

The model Eq. 16 is intractable as it stands, being a complex, strongly interacting many-body problem. We therefore proceed by utilizing the well-known mapping to a Kondo-type model, introduced first by Glazman and Matveev in Ref. [31] in the context of a single metallic island in a tunnel junction, and developed further in Refs. [29, 32, 72, 73]. The mapping consists of three steps.

The first step is to label the many-particle electronic states of the isolated but interacting islands described by $\mathcal{H}'_{\rm elec} + \mathcal{H}'_{\rm int}$ by their charge quantum numbers Q_α (which are conserved for $\mathcal{H}'_{\rm QPC} = 0$, and correspond to their U(1) labels). We write these states as $|\Psi_L;\Psi_R;Q_L;Q_R\rangle$, where Ψ_α is a state of island α with Q_α/e electrons, defined such that $\hat{Q}_\alpha|\Psi_L;\Psi_R;Q_L;Q_R\rangle = Q_\alpha|\Psi_L;\Psi_R;Q_L;Q_R\rangle$ for $\alpha = L, R$. The macroscopic number of electrons N_α on island α can be treated exactly as auxiliary degree of freedom, $|\Psi_L;\Psi_R;Q_L;Q_R\rangle \to |\Psi_L;\Psi_R\rangle_{\rm el} \otimes |N_L;N_R\rangle_{\rm ch}$ subject to the constraints $Q_\alpha = eN_\alpha$. The corresponding number operators in the charge subspace are defined as

$$\hat{N}_\alpha \;=\; \textstyle\sum_{n_L,n_R} n_\alpha \; |n_L;n_R\rangle\langle n_L;n_R|$$

such that $\hat{N}_L|n_L;n_R\rangle = n_L|n_L;n_R\rangle$ and $\hat{N}_R|n_L;n_R\rangle = n_R|n_L;n_R\rangle$. On the level of operators, this is equivalent to writing $\psi^\dagger_{\alpha\gamma k} = f^\dagger_{\alpha\gamma k}\hat{N}^+_\alpha$ and $\phi^\dagger_{\alpha k} = c^\dagger_{\alpha k}\hat{N}^+_\alpha$ (subject to the constraints $\hat{Q}_\alpha = e\hat{N}_\alpha$). Here, $f_{\alpha\gamma k}$ and $c_{\alpha k}$ are regular fermionic operators, while

$$\begin{aligned}\hat{N}^\pm_L &= \textstyle\sum_{n_L,n_R} \; |n_L \pm 1;n_R\rangle\langle n_L;n_R| \\ \hat{N}^\pm_R &= \textstyle\sum_{n_L,n_R} \; |n_L;n_R \pm 1\rangle\langle n_L;n_R|\end{aligned}$$

are ladder operators for the electron occupancy of the islands.

Since $\hat{N}^+_\alpha\hat{N}^-_\alpha = \sum_{n_L,n_R}|n_L;n_R\rangle\langle n_L;n_R| \equiv \hat{1}_{\rm ch}$ is the identity operator in the charge sector, we can identify $\mathcal{H}'_{\rm elec} \to \mathcal{H}_{\rm elec}$, with

$$\mathcal{H}_{\rm elec} = \sum_{\alpha,\gamma,k}\epsilon_k f^\dagger_{\alpha\gamma k}f_{\alpha\gamma k} + \sum_{\alpha,k}\epsilon_k c^\dagger_{\alpha k}c_{\alpha k}\;, \qquad (20)$$

which is equivalent to Eq. 4 in Methods. Furthermore, the constraint implies,

$$\mathcal{H}'_{\rm int} \to \mathcal{H}_{\rm int} = E^L_C\hat{N}^2_L + E^R_C\hat{N}^2_R + I\hat{N}_L\hat{N}_R\;, \qquad (21)$$

$$\mathcal{H}'_{\rm gate} \to \mathcal{H}_{\rm gate} = B'_L\hat{N}_L + B'_R\hat{N}_R\;. \qquad (22)$$

Including now the tunneling processes at the QPCs, we have

$$\begin{aligned}\mathcal{H}'_{\rm QPC} \to \mathcal{H}_{\rm QPC} = \sum_\alpha J_\alpha\left(f^\dagger_{\alpha l}f_{\alpha i}\hat{N}^-_\alpha + {\rm H.c.}\right) \\ + J_C\left(c^\dagger_L c_R\hat{N}^+_L\hat{N}^-_R + {\rm H.c.}\right)\;,\end{aligned} \qquad (23)$$

which accounts for quantum fluctuations in the number of electrons on the islands. For each tunneling event involving island α, the occupation N_α changes by ± 1. Everything is exact so far.

The second step is to relax the exact constraint $\hat{Q}_\alpha = e\hat{N}_\alpha$. This is an approximation, but one that is justified in the continuum limit [29, 31, 32, 72, 73], when the dynamics of $\hat{Q}_\alpha$ is insensitive to the precise number of electrons on the islands. For large metallic islands as used in the present experimental setup, each island hosts a very large number of electrons and the level spacing is small enough that the continuum approximation is valid even at experimental base temperatures. In this case, we can regard $\hat{N}_\alpha$ as *independent* degrees of freedom absorbed into the definition of a complex 'impurity' [73]. The states of the effective impurity (the island charge states) are interconverted by tunneling at the QPCs. The effective impurity model is given by $\mathcal{H} = \mathcal{H}_{\rm elec} + \mathcal{H}_{\rm QPC} + \mathcal{H}_{\rm int} + \mathcal{H}_{\rm gate}$ (Eqs. 20-23, without constraint). However, since the number of electrons on the islands is macroscopically large, the resulting impurity problem remains intractably complex.

The final step is therefore to project the full Hamiltonian $\mathcal{H}$ onto a simplified effective model $H_{\rm eff} = \hat{P}\mathcal{H}\hat{P}$ in which only a restricted set of island charge states are retained. This approximation is justified at low temperatures and small QPC transmissions, because excited charge states $\Delta E \sim \mathcal{O}(E^{L,R}_C)$ above the ground state become inaccessible for $k_BT \ll \Delta E$.

For a *single* metal island in a tunnel junction, the above steps yield an effective anisotropic Kondo model, when only the lowest two charge states are retained. The validity of this result was confirmed by Matveev and coworkers [31, 32], who showed that for small transmission the island charge and conductance exhibit periodic oscillations. Confining attention to a single such period in the vicinity of a charge-degeneracy point (Coulomb blockade step) in the ground state, the *full* model was projected onto an effective low-energy model in which only island states with N and $N+1$ electrons were retained (that is, $H_{\rm eff} = \hat{P}\mathcal{H}_{\rm full}\hat{P}$ with projector $\hat{P} = |N\rangle\langle N| + |N+1\rangle\langle N+1|$). It was shown in Ref. [32] that this effective model is indeed equivalent to the anisotropic Kondo model: a perturbative calculation of the scattering t-matrix found the same divergences at the charge degeneracy point of the island as in the spin-$\frac{1}{2}$ Kondo model with spin degeneracy. The connection was further demonstrated by a weak coupling renormalization group analysis [31, 32].

This charge-Kondo mapping is valid when only the lowest two charge states of the island play a role in the physics (the two active charge states being mapped to an 'impurity' pseudospin-$\frac{1}{2}$ degree of freedom). This model is therefore a good description of the physical system when the QPC transmissions are relatively small, temperature is relatively low, and the applied gate voltages do not push the system too far from the charge degeneracy point. If the QPC transmission becomes large, more island charge states become involved (and indeed near perfect QPC transmission, a macroscopic number of charge states become important and the Kondo-type description breaks down [29]). Likewise, at elevated temperatures $k_BT \sim \Delta E$ low-lying excited charge

states become important and cannot be neglected. Also, to capture the periodicity in gate voltage of the charge stability diagram, more charge states must be included in the effective model.

However, it is possible to relax the small transmission, small temperature, and small gate voltage conditions by going beyond the strict charge-Kondo model description to include more island charge states, as shown for the single-island case in [20, 73]. This allows quantitative comparisons to experiment at moderate transmission, though the experimentally-accessible limit of near-perfect transmission will always be beyond such a theoretical description [29]. Including more charge states also allows the physics at higher temperatures to be simulated, and to model the full charge stability diagram. For a given set of model parameters (transmissions, temperature, gate voltage etc) one can check that calculations are converged with respect to increasing the number of retained island charge states to give confidence that the model provides a faithful description of the physics.

Returning to the two-site system which is our focus here, we now discuss the mapping at low temperatures and weak QPC transmission in the vicinity of charge degeneracy points for both islands. Here we expect the mapping to result in a variant of the two-impurity Kondo model. Specifically, to obtain the DCK model Eq. 1, we project the Hamiltonian $\mathcal{H}$ onto the four-dimensional manifold of charge states:
$(n,m) = (N,M), (N+1,M), (N,M+1), (N+1,M+1)$
where N and M are suitable reference macroscopic charge states of each island. For small applied gate voltages ($B_L, B_R \ll \Delta E$), these states can be selected as the low-energy (ground state) manifold by setting the offsets $B_L^0 = -2E_C^L(N+\frac{1}{2}) - I(M+\frac{1}{2})$ for the left island and $B_R^0 = -2E_C^R(M+\frac{1}{2}) - I(N+\frac{1}{2})$ for the right island. All other charge states are at least $E_C^{L,R}$ higher in energy. Zero applied gate voltage $B_L = B_R = 0$, then corresponds to the charge degeneracy point for the individual islands ($J_\alpha = 0$ and $I = 0$); while $B_L = B_R = 0$ yields the high-symmetry point between triple points in the charge stability diagram of the full system (finite J_α and I). In this case,

$$\begin{aligned}\mathcal{H}_{\rm int} + \mathcal{H}_{\rm gate} &= E_C^L(\hat{N}_L - N - \tfrac{1}{2})^2 + E_C^R(\hat{N}_R - M - \tfrac{1}{2})^2 \\ &+ I(\hat{N}_L - N - \tfrac{1}{2})(\hat{N}_R - M - \tfrac{1}{2}) + B_L\hat{N}_L + B_R\hat{N}_R \end{aligned} \quad (24)$$

We directly obtain $H_{\rm DCK} = \hat{P}\mathcal{H}\hat{P}$ with projector $\hat{P} = \sum_{a,b\in 0,1} |N+a; M+b\rangle\langle N+a; M+b|$, up to irrelevant constants. The projection becomes exact in the limit $E_C^{L,R} \to \infty$. In Eq. 1 we now identify the charge pseudospin-$\frac{1}{2}$ operators as:

$$\begin{aligned}\hat{\mathcal{S}}_L^+ &= \sum_{b=0,1} |N+1; M+b\rangle\langle N; M+b| \,, \\ \hat{\mathcal{S}}_L^z &= \tfrac{1}{2}\sum_{b=0,1} \Big[|N+1; M+b\rangle\langle N+1; M+b| \\ &\qquad -|N; M+b\rangle\langle N; M+b|\Big] \,,\end{aligned}$$

and $\hat{\mathcal{S}}_L^- = \left(\hat{\mathcal{S}}_L^+\right)^\dagger$ for the left island, whereas,

$$\begin{aligned}\hat{\mathcal{S}}_R^+ &= \sum_{a=0,1} |N+a; M+1\rangle\langle N+a; M| \,, \\ \hat{\mathcal{S}}_R^z &= \tfrac{1}{2}\sum_{a=0,1} \Big[|N+a; M+1\rangle\langle N+a; M+1| \\ &\qquad -|N+a; M\rangle\langle N+a; M|\Big] \,,\end{aligned}$$

and $\hat{\mathcal{S}}_R^- = \left(\hat{\mathcal{S}}_R^+\right)^\dagger$ for the right island.

The effective low-energy DCK model is a variant of the standard spin-$\frac{1}{2}$ two-impurity Kondo model, here with anisotropic exchange, but also with the dynamics of an additional conduction electron bath in the central region correlated to the inter-impurity interaction – a kind of two-impurity, three channel model. Separate island-lead Kondo effects now compete with an inter-island Kondo effect, giving rise to a quantum phase transition, as discussed in the main text and confirmed by experimental conductance measurements.

Periodicity of system

The DCK model is expected to hold equivalently near any triple point. Experimentally, by sweeping over a larger gate voltage range than shown in the main text, we see a periodic structure with no systematic differences at any given pair of triple points. Any averaging done was in fact over different pairs of triple points, as the positions of each triple point in gate voltage space drift over time. In Supplementary Fig. 6 we show one example of a measured charge stability diagram over a large range of U_L, U_R. This particular measurement additionally displays two representative types of charge noise – occasional jumps of a clear discontinuity and more scattered individual points of noise.

Single Island Two-Channel Kondo

A key assumption in our present work is that both the left and the right island are each a true implementation of a charge-Kondo site. We reproduced a key earlier experimental demonstration of two-channel Kondo behavior by Iftikhar [19], which is only possible with a true equivalent recreation of the hybrid metal-semiconductor island. Shown in Supplementary Fig. 7 is the series conductance through a single island ($\tau_C = 0$), rescaled into a universal conductance curve as a function of T/T_K. T_K is determined by the transmissions of two island-lead QPCs (for example, τ_R, and the opposite QPC of the right island, unlabeled in Fig. 1a) which are set to be equal. To best compare results, we set the same transmissions ($\tau = \{.06, 0.12, 0.245, 0.36, 0.47, 0.57, 0.68, 0.77, 0.85, 0.93\}$) as in [19], and thus nearly the same T_K values (due to the similar charging energies E_C in the two experiments). A caveat in our system however, is that we could only see quantitative agreement when using values for QPC transmissions renormalized by dynamical Coulomb blockade as described in Methods.

REFERENCES

[66] Jayaprakash, C., Krishna-murthy, H. R. & Wilkins, J. W. Two-Impurity Kondo Problem. *Phys. Rev. Lett.* **47**, 737–740 (1981).

[67] Affleck, I. & Ludwig, A. W. W. Exact critical theory of the two-impurity Kondo model. *Phys. Rev. Lett.* **68**, 1046–1049 (1992).

[68] Simon, P., López, R. & Oreg, Y. Ruderman-Kittel-Kasuya-Yosida and Magnetic-Field Interactions in Coupled Kondo Quantum Dots. *Phys. Rev. Lett.* **94**, 086602 (2005).

[69] Mitchell, A. K. & Sela, E. Universal low-temperature crossover in two-channel Kondo models. *Phys. Rev. B* **85**, 235127 (2012).

[70] Mitchell, A. K., Sela, E. & Logan, D. E. Two-Channel Kondo Physics in Two-Impurity Kondo Models. *Phys. Rev. Lett.* **108**, 086405 (2012).

[71] Albrecht, S. M. *et al.* Exponential protection of zero modes in Majorana islands. *Nature* **531**, 206–209 (2016).

[72] Schoeller, H. & Schön, G. Mesoscopic quantum transport: Resonant tunneling in the presence of a strong coulomb interaction. *Physical Review B* **50**, 18436 (1994).

[73] Lebanon, E., Schiller, A. & Anders, F. B. Coulomb blockade in quantum boxes. *Physical Review B* **68**, 041311 (2003).

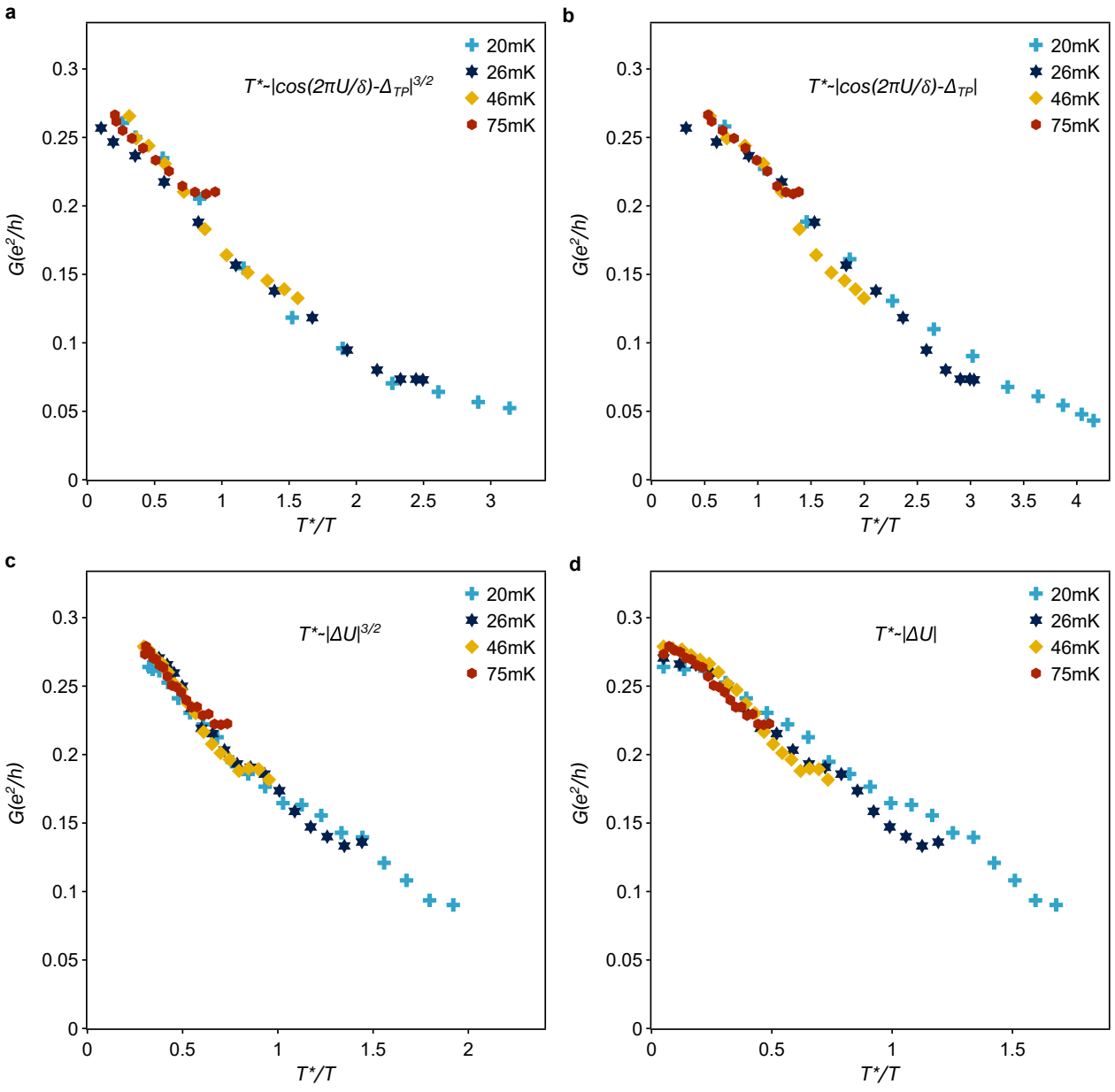

Supplementary Fig. 1: Analysis of alternative power law. a. Scaling collapse of the same data in Fig. 3b without the universal curve. **b.** Same data as in **a**, but with $|\cos(2\pi U/\delta) - \Delta_{TP}|$ raised to a power of 1 instead of 3/2. Other reasonable choices for the exponent such as $1/2$ or 2 do not show clear collapse onto a single curve. **c.** We also show the data of Fig. 3c without the universal curve, and similarly compare the same data plotted using $T^* \sim |\Delta U|^1$ in **d**, which likewise shows poorer scaling collapse.

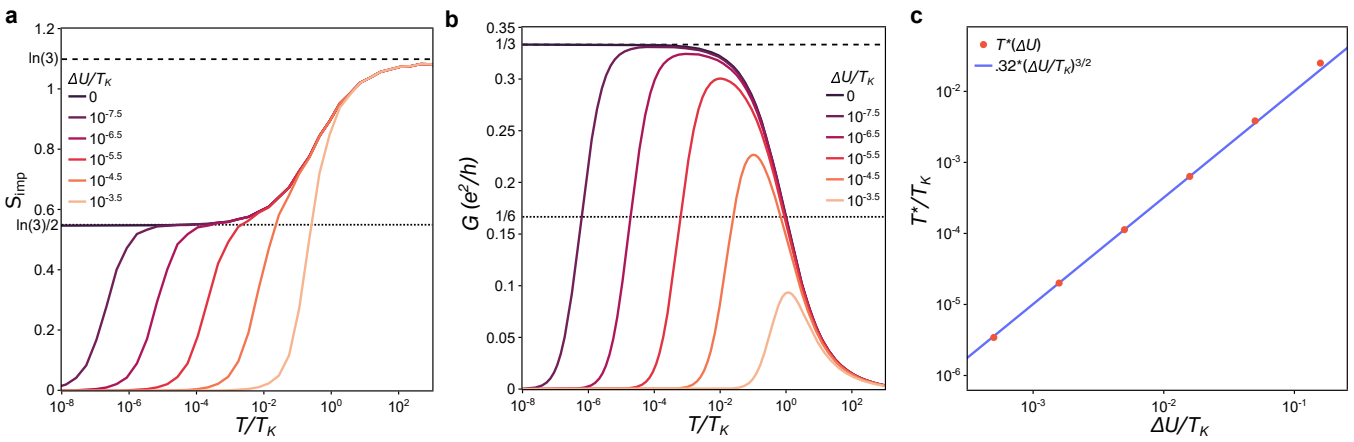

Supplementary Fig. 2: Physical properties near the near critical point. a, The NRG calculated entropy flow as a function of T/T_K. The different colors represent different values of triple point detuning ΔU, which controls the Fermi liquid scale T^*, limiting the range of temperature for which the non-trivial $\ln(\sqrt{3})$ entropy is predicted. **b,** NRG calculated series conductance as a function of T/T_K, for the same ΔU values as in **a**. For small ΔU we see good scale separation $T^* \ll T_K$, in which case we have effectively two universal conductance curves – one approaching the critical point as a function of T/T_K and the other Fermi liquid crossover away from the critical point as a function of T/T^*. The latter is probed experimentally in this work. **c,** The NRG calculated Fermi-liquid scale T^* (in units of T_K, red points) plotted against $\Delta U/T_K$. This is compared to the asymptotic behavior near the triple point used in Eq. 2 where $T^* \sim |\Delta U|^{3/2}$ (blue line). Note that similar behavior is observed for detuning the couplings $J_{L,R} \neq J_C$ away from the critical point.

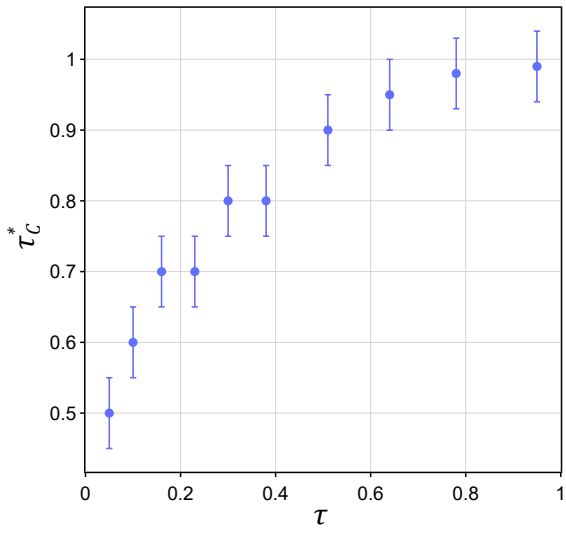

Supplementary Fig. 3: Competition between Kondo interactions. Conductance enhancement is greatest when the island-lead and inter-island Kondo interactions are of equal strength, which is seen as an increasing τ_C^* as τ is increased. τ_C^* is determined as the τ_C value for which conductance is a maximum, regardless of U. This value defines the plotted circles. In the data set these values are extracted from, τ_C is stepped by 0.1. Thus, we can only reliably identify τ_C* within an uncertainty of ± 0.1, represented by the error bars. The non-linear relation is likely due to both $\tau = \tau_C$ not implying $J = J_C$ and a difference in how we are able to measure τ and τ_C (Methods).

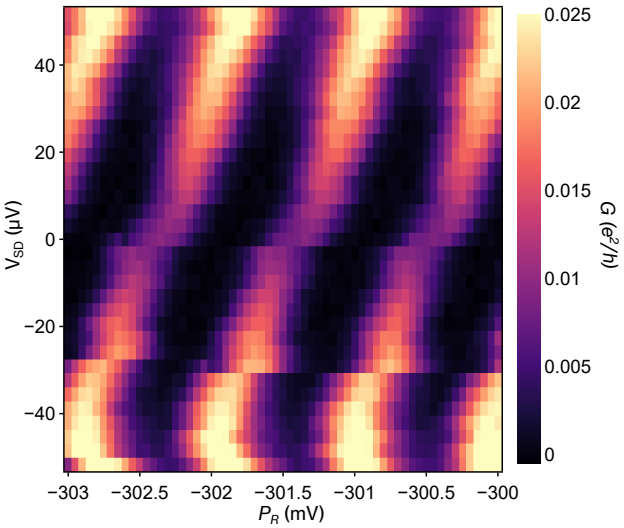

Supplementary Fig. 4: Coulomb diamonds. Conductance measurement through a single island ($\tau_C = 0$) as a function of the plunger gate P_R and a source-drain bias V_{SD}. The height of the diamond is used to extract $E_C \approx 25$ μeV, and subsequently a lever arm $\alpha = 50$ μeV/mV to convert gate voltages to energies.

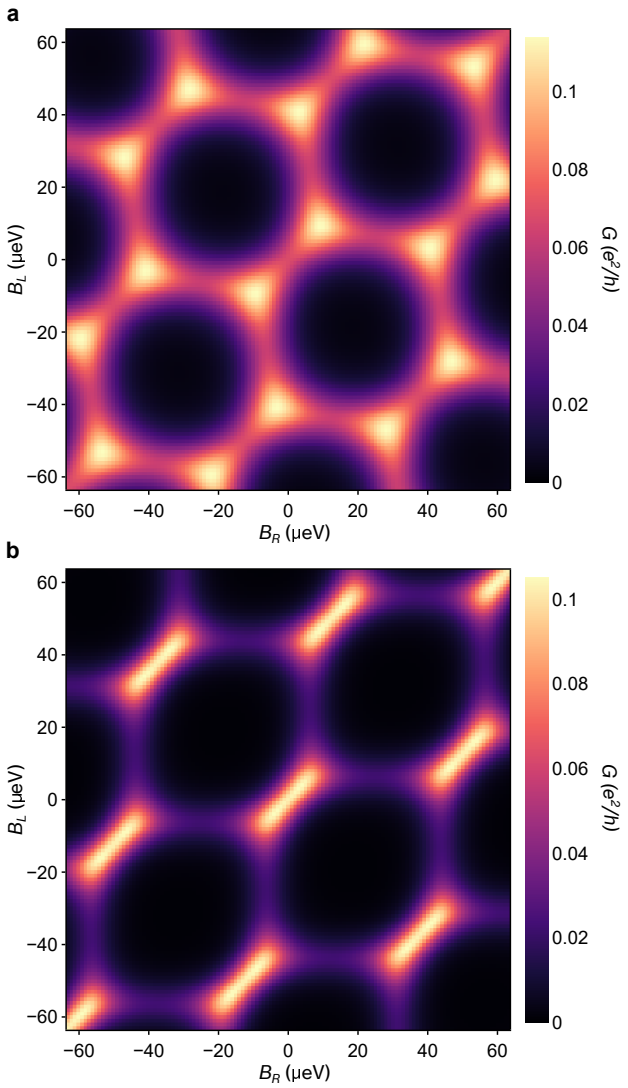

Supplementary Fig. 5: Unskewed NRG charge stability diagram. Charge stability diagrams of Fig. 1d as a function of B_L, B_R.

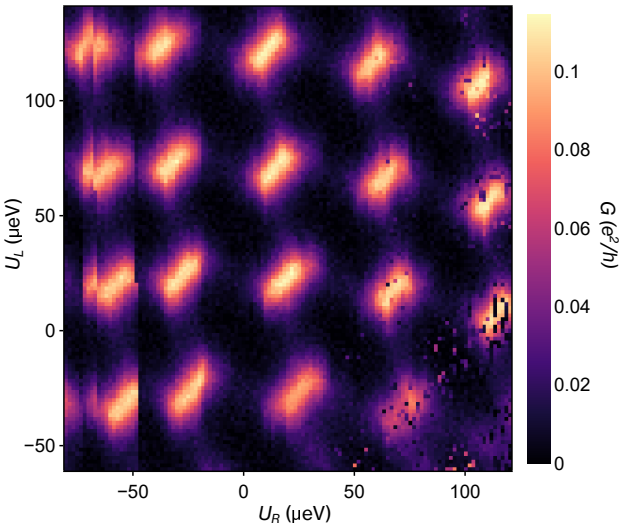

Supplementary Fig. 6: Periodicity of charge stability diagram. The bottom charge stability diagram of Fig. 1c over a broader range of U_L, U_R showing the periodicity. This also shows the two representative types of charge noise which affect measurements – occasional jumps (on the left side) where there is a clear vertical discontinuity, and more scattered individual points of noise (on the far right).

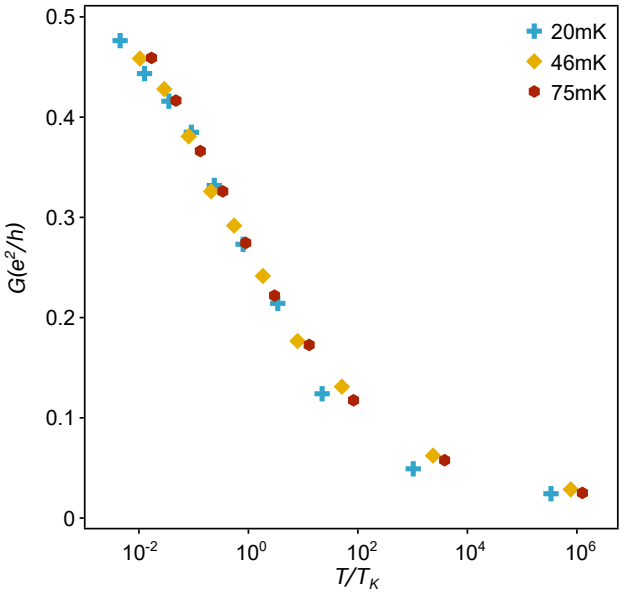

Supplementary Fig. 7: Two-channel Kondo scaling for a single island. The measured series conductance through a single island ($\tau_C = 0$), with equal transmissions set for the top and bottom island-lead QPC. The transmissions are rescaled into a Kondo temperature, and when the conductance is plotted as a function of the single parameter T/T_K, they fall onto a single universal curve.